Analysis of 3D solids using the natural neighbour radial point interpolation method

L.M.J.S. Dinis [a,*], R.M. Natal Jorge [a,1], J. Belinha [b,2]

[a] *Faculty of Engineering of the University of Porto, FEUP, Rua Dr. Roberto Frias, 4200-465 Porto, Portugal*
[b] *IDMEC, Institute of Mechanical Engineering, Rua Dr. Roberto Frias, 4200-465 Porto, Portugal*

Abstract

In this work an improved meshless method is proposed, based on the combination of the natural neighbour finite element method with the radial point interpolation method, the natural neighbour radial point interpolation method – NNRPIM. The nodal connectivity and the node dependent integration background mesh are constructed resorting to the Voronoï tessellation and to the Delaunay triangulation. Within NNRPIM the obtained shape functions pass through all nodes inside the influence-cell providing shape functions with the delta Kronecker property. Optimization tests and examples of well-known, 2D and 3D problems are solved in order to prove the high accuracy and convergence rate of the proposed method.
© 2006 Elsevier B.V. All rights reserved.

1. Introduction

The finite element method (FEM) is a well-known numerical method [1,2], which has been applied to different engineering fields and to distinct applied sciences. The domain of the problem is divided into small elements and the field function is interpolated within each element by simple interpolation functions, the so called shape functions. However in the case of complex geometries the generation of highly distorted elements is common. The distortion of elements causes low quality shape functions which can affect the performance of the method.

In the meshless methods [3,4] the nodes can be arbitrary distributed, once the field functions are approximated within an influence domain rather than an element. In

opposition to the no-overlap rule between elements in the FEM, in meshless methods the influence domains may and must overlap each other.

The diffuse element method (DEM) [5] was the first meshless method that uses the moving least square approximants (MLS) in the construction of the approximation function. The MLS was proposed by Lancaster and Salkauskas [6] for surface fitting. Belytschko evolved the DEM and developed one of the most popular meshless method, the element free Galerkin method (EFGM) [7–9]. The smooth particle hydrodynamics method (SPH) [10], which is one of the oldest, it is in the origin of the reproducing kernel particle method (RKPM) [11]. Other meshless methods such as the meshless local Petrov–Galerkin method (MLPG) [12], the finite point method (FPM) [13] and the method of finite spheres (FSM) [14] were developed as well.

Although these meshless methods have been successfully applied in computational mechanics there are several problems not completely solved. One of these problems, and perhaps the most important unsolved issue, is the imposition of essential and natural boundary conditions, due to

---

* Corresponding author. Tel.: +351 225081593/1716; fax: +351 225081584.
 E-mail addresses: ldinis@fe.up.pt (L.M.J.S. Dinis), rnatal@fe.up.pt (R.M. Natal Jorge), jorge.belinha@fe.up.pt (J. Belinha).
[1] Tel.: +351 225081720/1716; fax: +351 225081584.
[2] Tel.: +351 225081491/1571; fax: +351 225081538.

the lack of the delta Kronecker property, $\varphi_i(\mathbf{x}_j) \neq \delta_{ij}$. This is the immediate consequence, in the referred meshless methods, of using approximation functions instead of interpolation functions.

To address the above problem several new meshless methods were developed in the last few years, the point interpolation method (PIM) [15,16], the point assembly method [17], the natural neighbour finite elements method (NNFEM) [18,19] or natural element method (NEM) [20–23] and the meshless finite element method (MFEM) [24].

The PIM is a very attractive method. The approximation functions are in fact interpolation functions, consequently generating shape functions with the delta Kronecker property. The construction of the shape functions is simple, compared with the EFGM, and its derivatives are easily obtained. The PIM evolved, and instead of using the original polynomial basis function, it was proposed in [25] and successfully applied in [26], the use of the radial basis function for solving partial differential equations. This combination allows the generation of the radial point interpolation method (RPIM). The radial basis functions used in these early works were the Gaussian and the multiquadric radial basis functions.

Initially the radial basis function was developed for data surface fitting, and later, with the work developed by Kansa [27], the radial basis function was used for solving partial differential equations. However Kansa's algorithm uses the concept of "global domain" instead of "influence domain", as the recently proposed LS-RPCM [28]. The RPIM also uses the concept of "influence domain", as the LS-RPCM, generating sparse and banded stiffness matrices, more adequated to complex geometry problems. The RPIM was also extended to the three-dimensional analysis [29] and successfully applied to problems with smart materials [30–32] and plate and shell structures [33–37].

The NEM is currently one of the most popular and discussed meshless method. In the NEM the trial and test functions are constructed using natural neighbour interpolants [38]. The natural neighbour interpolants represent a multivariate data interpolation scheme which has been initially used in data fitting. To construct the interpolation function the natural neighbour interpolants rely on geometrical and mathematical concepts such as the Voronoï diagrams [39] and the Delaunay tessellation [40].

Another important issue is the need of a background mesh for integration purposes. In fact a meshless method is not a truly mesh free method, if it relies in a secondary background integration mesh. Nevertheless the general idea [41] is that truly meshless methods, methods that do not require any mesh at all, are less stable and less accurate.

In this paper the analysis of 2D and 3D solid mechanics problems is performed resorting to an improved meshless method [42,43], the Natural neighbour radial point interpolation method – NNRPIM. Resorting to Voronoï cells, a set of influence cells are created departing from an unstructured set of nodes. The Delaunay triangles, which are the dual of the Voronoï cells, are used to create a node-depending background mesh used in the numerical integration of the NNRPIM interpolation functions. Unlike the FEM, where geometrical restrictions on elements are imposed for the convergence of the method, in the NNRPIM there are no such restrictions, which permits a total random node distribution for the discretized problem. The NNRPIM interpolation functions, used in the Galerkin weak form, are constructed in a similar process to the RPIM, with some differences that modify the method performance.

In the NNRPIM a displacement-based Galerkin implementation is used, in order to obtain and solve the equilibrium equation of elastostatics. The solution of the discrete linear system of equations is carried out to obtain the nodal displacement vector, $\mathbf{u} = \mathbf{k}^{-1}\mathbf{f}$.

The outline of the paper is as follows: In Section 2 the construction of the NNRPIM influence-cells is presented and the new integration schemes that are used in this work are proposed. In Section 3 the construction of the NNRPIM interpolation functions is presented. In Section 4 the NNRPIM formulation for elastostatics is developed. In Section 5 the NNRPIM is implemented, optimal shape parameters are obtained and several well-known 2D and 3D problems are solved. This work ends with the conclusions and remarks in Section 6.

2. Natural neighbours

The concept of natural neighbours was firstly introduced by Sibson [44] for data fitting and smoothing. The Voronoï diagrams and the Delaunay triangulation are useful mathematical tools in the determination of the natural neighbours for each node belonging to the global nodal set. This theory is applicable to a $\mathscr{D}$-dimensional space, however for simplicity in this work an example of a two-dimensional Euclidian space $\mathbb{R}^2$ is presented. Consider a set $\mathbf{N}$ of N distinct nodes,

$$\mathbf{N} = \{n_1, n_2, \ldots, n_N\} \in \mathbb{R}^2. \tag{1}$$

The Voronoï diagram of $\mathbf{N}$ is the partition of the domain defined by $\mathbf{N}$ in sub-regions V_I, closed and convex. Each sub-region V_I is associated to the node I, n_I, in a way that any point in the interior of the V_I is closer to n_I than any other node n_J, where $n_J \in N(J \neq I)$. In other words, V_I is the geometric place where all points are closer to n_I than to any other node. The sub-regions V_k are the "Voronoï cells" which form the Voronoï diagram, $k = 1, \ldots, N$. In mathematical terms the Voronoï cell is defined by,

$$V_I = \{x \in \mathbb{R}^2 : \mathscr{E}_n(\mathbf{x}, \mathbf{x}_I) < \mathscr{E}_n(\mathbf{x}, \mathbf{x}_J) \forall J \neq I\} \tag{2}$$

being $\mathscr{E}_n(\mathbf{x}_J, \mathbf{x}_I)$, the Euclidian metric norm, i.e., the distance between points with coordinates defined by $\mathbf{x}_J$ and $\mathbf{x}_I$. In Fig. 1(a)–(d) the construction of the sub-region V_I is represented, which starts with a nodal set of potential neighbours represented in Fig. 1(a). As Fig. 1(b) indicates the neighbour nodes are obtained by the intersection of
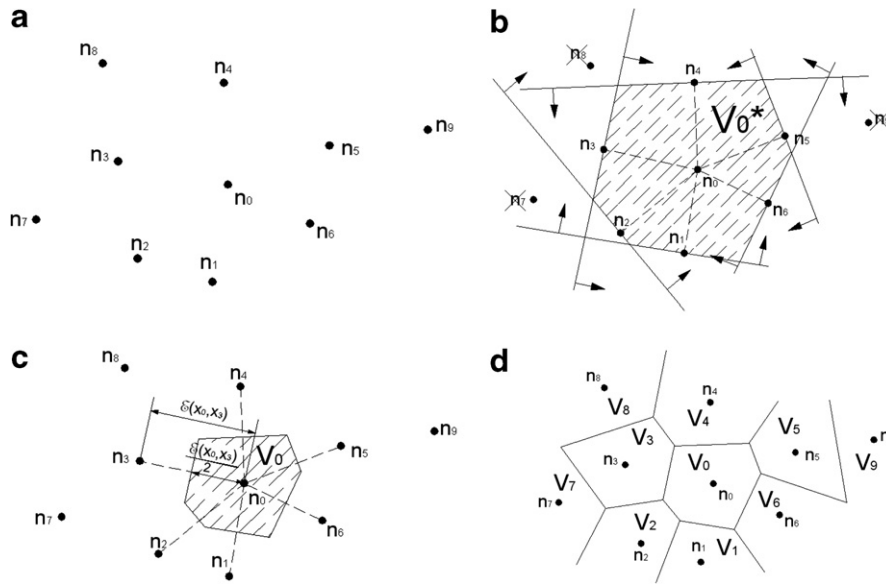
Fig. 1. (a) Initial nodal set of potential neighbour nodes, (b) final cell containing only neighbour nodes, (c) Voronoï cell and (d) Voronoï diagram.

domains whose limits are defined by the line that intersects node J (potential neighbour node) and is normal to the dashed line $0J$, where 0 is the interest or central node. By definition, only the nodes in the perimeter of the obtained final domain, V_0^*, are considered as neighbour nodes. The Voronoï cell, V_0, obtained is determined as Fig. 1(c) indicates. The cell V_0 is the homothetic form of V_0^*. A similar procedure is applied in order to obtain the remaining Voronoï cells, Fig. 1(d).

The Delaunay triangulation is the geometrical dual of the Voronoï diagram and it is constructed by connecting the nodes whose Voronoï cells have common boundaries. The duality between the Voronoï diagram and the Delaunay triangulation implies that a Delaunay edge exists between two nodes in the plane if and only if their Voronoï cells share a common edge.

An important property of the Delaunay triangles is the "empty circumcircle criterion" [45]. If a set of nodes $N_t = \{ n_J \quad n_K \quad n_L \} \in N$ forms a Delaunay triangle then the circumcircle formed by the triangle N_t contains no other nodes of N. In the context of the natural neighbour interpolation these circles are known as "natural neighbour circumcircles" [46]. The centre of the natural neighbour cir-

cumcircle is the vertex of the respective Voronoï cell. These features are presented in Fig. 2.

In this work the Voronoï diagram is used to create the "influence-cells", which enforces the connectivity between the nodes in N. On the other hand the duality between the Voronoï cells and the Delaunay triangles is used in order to construct a nodal dependent background integration mesh.

2.1. Influence-cells and nodal connectivity

In works related with the RPIM [25,26] the nodal connectivity is obtained by the overlap of the influence domain of each node. These influence domains are found by searching enough nodes inside a fixed area or a fixed volume, respectively for the 2D problem and for the 3D problem. Because of its simplicity many other meshless methods use this concept [7,11,12,15]. However the size or shape variation of these influence domains along the problem domain affects the performance and the final solution of the meshless method. It is important that all the influence domains in the problem contain approximately the same number of nodes. In this work the nodal connectivity is
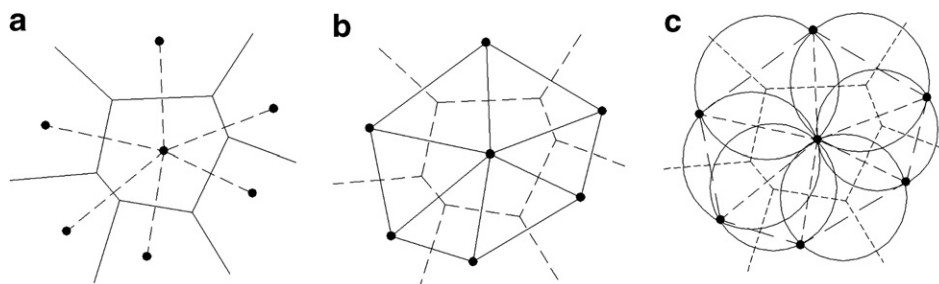

Fig. 2. (a) Initial Voronoï diagram, (b) Delaunay triangulation and (c) natural neighbour circumcircles.
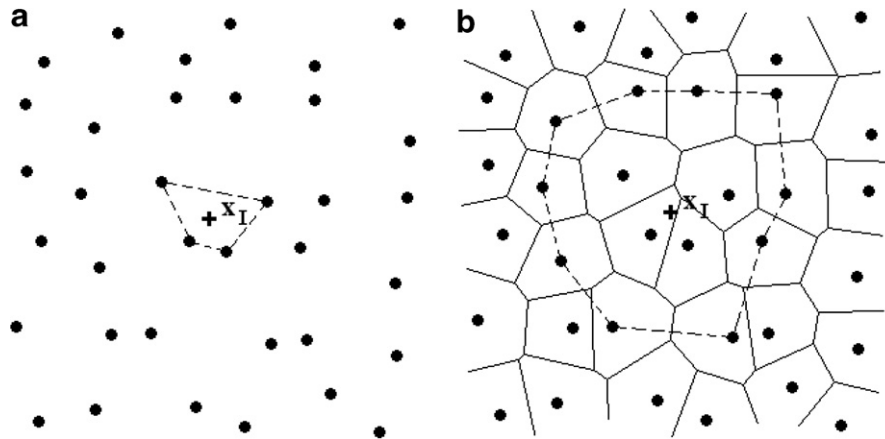
Fig. 3. (a) First degree influence-cell and (b) second degree influence-cell.

imposed by the overlapping of the influence-cells [42,43], which can be considered as a new concept, similar to the influence domain, which is obtained from the Voronoï cells. The cell formed by n nodes that contributes to the interpolation of the interest point $\mathbf{x}_I$ is called "influence-cell". Since it is simpler to represent, only the determination of the 2D influence-cell is presented, however this concept is applicable to a $\mathscr{D}$-dimensional space. Two distinct types of influence-cells are presented.

First degree influence-cell: A point of interest, $\mathbf{x}_I$, searches for its neighbour nodes, Fig. 3(a), following the Natural Neighbour Voronoï construction presented early. Thus the *first degree influence-cell* is composed by these first natural neighbours.

Second degree influence-cell: A point of interest, $\mathbf{x}_I$, searches for its neighbour nodes, in the same manner as in the *first degree influence-cell*. Then, based on a previous construction of the Voronoï diagram for the node mesh, the natural neighbours of the first natural neighbours of $\mathbf{x}_I$ are added to the influence-cell, Fig. 3(b).

In an initial phase, after the domain discretization in a regular or an irregular nodal mesh, the Voronoï cells of each node are constructed. These cells can be considered as a background mesh for integration purpose, being determined the influence-cell for each one of these integration points.

2.2. Numerical integration in the NNRPIM

Recently the RPIM based on stabilized nodal integration [47] was successfully implemented and the obtained results proved to be better than the RPIM based on Gauss integration schemes. In this work another integration scheme based on the Voronoï tessellation and the Delaunay triangulation is proposed. Using the referred constructions small areas are established, which can be quadrilaterals or triangles consistent with an irregular or a regular mesh respectively. Then, with the construction of the Voronoï cells, V_I, the intersection points, P_{Ii}, of the neighbour edges of V_I can be settled, Fig. 4(a). After-

wards the middle points, M_{Ii}, between node *I* and its neighbour nodes are obtained. Thus the Voronoï cells are divided in *n* quadrilateral sub-cell, S_{Ii}, as Fig. 4(b) and (c) indicate.

For the regular mesh, Fig. 4(d)–(f), the middle points M_{Ii} are coincident with the edge intersection points P_{Ii}. It is visible that this geometric coincidence leads to the formation of triangles instead of the quadrilateral sub-cells, as in the irregular mesh.

Any Voronoï cell, V_I, with *n* neighbour nodes of the central node *I* has *n* sub-cells, S_{Ii}, where

$$A_{V_I} = \sum_{i=1}^{n} A_{S_{Ii}}, \quad \forall A_{S_{Ii}} \geqslant 0 \tag{3}$$

being A_{V_I} the Voronoï cell area and $A_{S_{Ii}}$ the sub-cell area. If the set of Voronoï cells are a partition, without gaps, of the global domain then, the set of sub-cells are also a partition, without gaps, of the global domain. It is clear now how the construction of the sub-cells generates two types of basic shapes – triangles or quadrilaterals. Starting with these two shapes, numerous integrations schemes can be constructed. In this work it is proposed an ordered scheme, based on the Gauss–Legendre numerical integration.

2.2.1. Integration scheme – order 0

The coordinates of each integration point are calculated on each sub-cell, as indicated in Fig. 5(a) and (d), where $\mathbf{x}_i = \{x_i, y_i\}$. The weight of each integration point is the area of the respective sub-cell. Therefore, considering Fig. 5(d), the area of the triangle shape sub-cell is defined by

$$A_I\triangle = \text{abs}\left(\frac{1}{2}\begin{vmatrix} x2 - x1 & y2 - y1 \\ x3 - x1 & y3 - y1 \end{vmatrix}\right) \tag{4}$$

and for the quadrilateral shape, Fig. 5(a), the area is

$$A_I\square = \text{abs}\left(\frac{1}{2}\begin{vmatrix} x2 - x1 & y2 - y1 \\ x3 - x1 & y3 - y1 \end{vmatrix} + \frac{1}{2}\begin{vmatrix} x4 - x1 & y4 - y1 \\ x3 - x1 & y3 - y1 \end{vmatrix}\right). \tag{5}$$
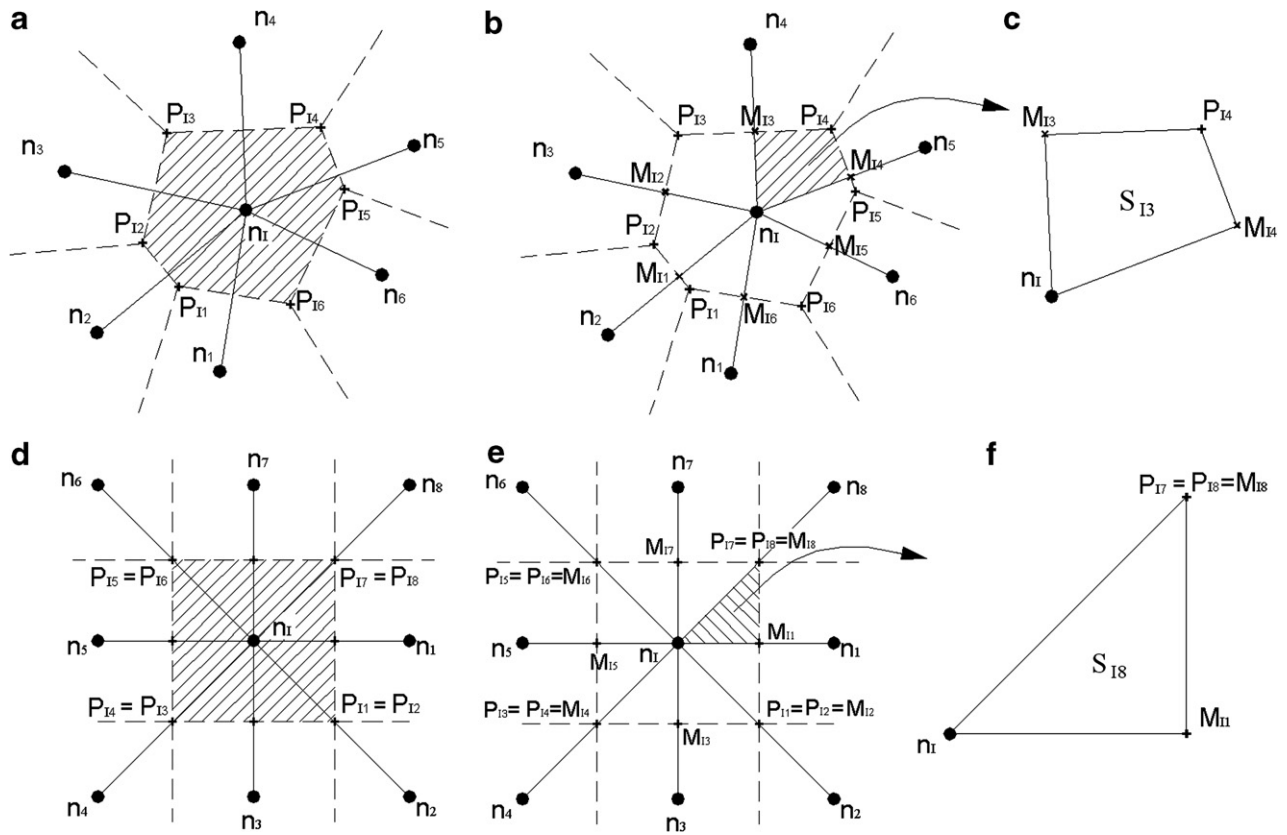
Fig. 4. For the irregular mesh (a) Voronoï cell and the respective P_{Ii} intersection points, (b) middle points M_{Ii} and the respective generated quadrilaterals, (c) quadrilateral $\overline{M_{I3}P_{I4}M_{I4}n_I}$. For the regular mesh, (d) Voronoï cell and the respective P_{Ii} intersection points, (e) middle points M_{Ii} and the respective generated triangles and (f) triangle $\overline{P_{I8}M_{I1}n_I}$.
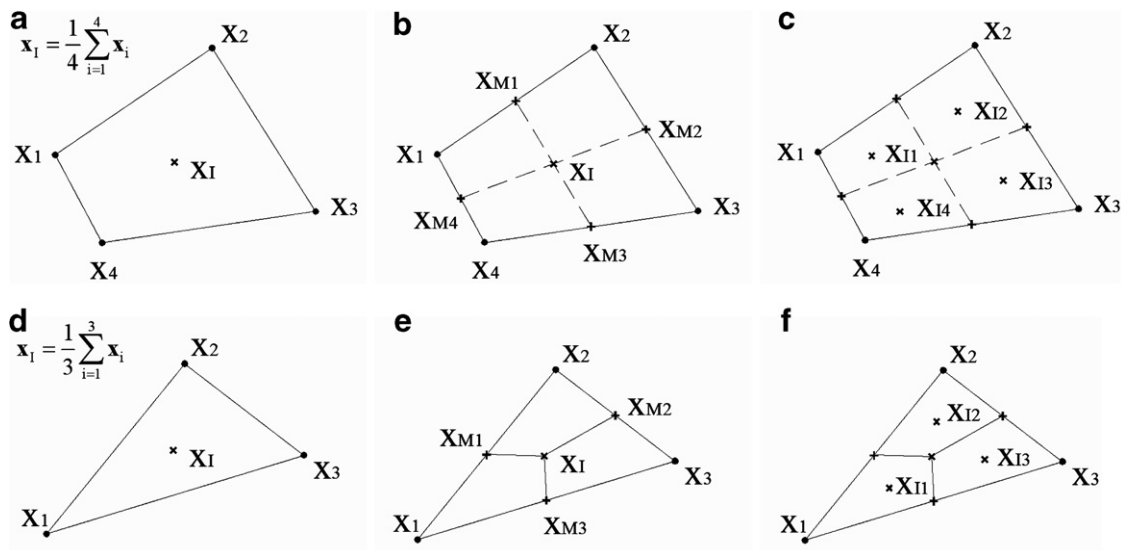

Fig. 5. (a) Quadrilateral shape and (d) triangular shape and the respective integration points $\mathbf{x}_I$, (b) and (e) partition of the initial shape into quadrilaterals, (c) and (f) respective integration points $\mathbf{x}_I$.

The process is the same as the 1×1 integration point Gauss–Legendre scheme for triangle and quadrilateral shapes, respectively.

2.2.2. Integration scheme – order 1

In this integration scheme the basic geometric forms are sub-divided again. However, in this case only in quadrilat-
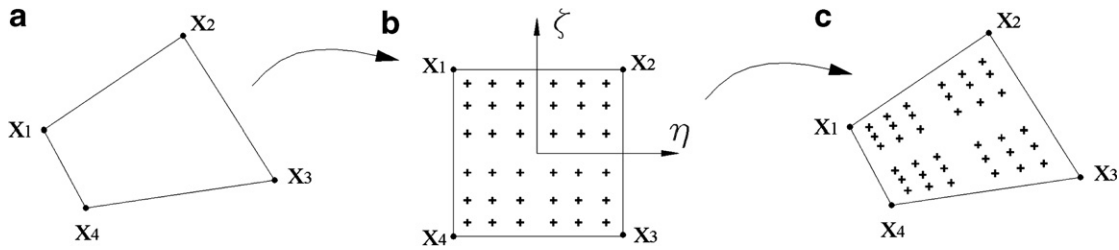
Fig. 6. (a) Initial quadrilateral, (b) transformation of the initial quadrilateral into an isoparametric square shape and application of the 6×6 quadrature point rule and (c) return to the initial quadrilateral shape.

eral shapes, as Fig. 5(b) and (e) indicate. Firstly, the centre of the geometric shape is determined, afterwards middle points on the edges are determined and then new quadrilaterals are constructed.

For each new quadrilateral shape obtained the "Integration scheme of order 0" is applied, Fig. 5(c) and (f).

2.2.3. Integration scheme – order k

Considering the quadrilateral shapes constructed for the "Integration scheme of order 1" a Gauss–Legendre quadrature scheme of $k \times k$ integration points is applied, Fig. 6.

The integration weight is defined by

$$A_I = w_\eta w_\zeta \left(\frac{A\square}{4} \right), \tag{6}$$

where $A\square$ is defined in Eq. (5), w_η and w_ζ are the Gauss quadrature weights for an isoparametric quadrilateral element.

The extension of the presented 2D integration scheme is strait-forward for the 3D space. In the irregular mesh, the Voronoï cell is subdivided in hexahedrons and in the regular mesh in tetrahedrons. Then the distinct integration scheme orders are obtained following the 2D procedure.

3. Shape function construction

In the meshless methods several techniques have been developed in order to obtain the shape functions. Some of these techniques construct approximation functions, as for example the EFGM [7], the RKPM [11] and the MLPG [12]. The great disadvantage of the approximation functions is the lack of the delta Kronecker property, which makes the imposition of the essential and natural boundary conditions difficult.

This work uses the junction of two well known methods, the moving least-square approximants (MLS) [6] and the radial point interpolators (RPI) [25,26].

Consider a function $\mathbf{u}(\mathbf{x})$ defined in the domain Ω, which is discretized by a set of N nodes. It is assumed that only the nodes within the influence-cell of the point of interest $\mathbf{x}_I$ have effect on $\mathbf{u}(\mathbf{x}_I)$. The value of function $\mathbf{u}(\mathbf{x}_I)$ at the point of interest $\mathbf{x}_I$ is obtained by

$$\mathbf{u}(\mathbf{x}_I) = \sum_{i=1}^{n} R_i(\mathbf{x}_I) a_i(\mathbf{x}_I) + \sum_{j=1}^{m} p_j(\mathbf{x}_I) b_j(\mathbf{x}_I) = \{\mathbf{R}^{\mathrm{T}}(\mathbf{x}_I), \mathbf{p}^{\mathrm{T}}(\mathbf{x}_I)\} \begin{Bmatrix} \mathbf{a} \\ \mathbf{b} \end{Bmatrix}, \tag{7}$$

where $R_i(\mathbf{x}_I)$ is the radial basis function (RBF), n is the number of nodes inside the influence-cell of $\mathbf{x}_I$. The coefficients $a_i(\mathbf{x}_I)$ and $b_j(\mathbf{x}_I)$ are non constant coefficients of $R_i(\mathbf{x}_I)$ and $p_j(\mathbf{x}_I)$, respectively. The monomials of the polynomial basis are defined by $p_j(\mathbf{x}_I)$ and m is the basis monomial number. The vectors in Eq. (7) are defined as

$$\begin{aligned}
\mathbf{R}^{\mathrm{T}}(\mathbf{x}_I) &= \{R_1(\mathbf{x}_I), R_2(\mathbf{x}_I), \dots, R_n(\mathbf{x}_I)\}, \\
\mathbf{p}^{\mathrm{T}}(\mathbf{x}_I) &= \{p_1(\mathbf{x}_I), p_2(\mathbf{x}_I), \dots, p_m(\mathbf{x}_I)\}, \\
\mathbf{a}^{\mathrm{T}}(\mathbf{x}_I) &= \{a_1(\mathbf{x}_I), a_2(\mathbf{x}_I), \dots, a_n(\mathbf{x}_I)\}, \\
\mathbf{b}^{\mathrm{T}}(\mathbf{x}_I) &= \{b_1(\mathbf{x}_I), b_2(\mathbf{x}_I), \dots, b_m(\mathbf{x}_I)\}.
\end{aligned} \tag{8}$$

In the RBF the variable is the distance r_{Ii} between the relevant node $\mathbf{x}_I$ and the neighbour node $\mathbf{x}_i$. For the three-dimensional space: $r_{Ii} = \sqrt{(x_I - x_i)^2 + (y_I - y_i)^2 + (z_I - z_i)^2}$. Several known RBFs are well studied and developed in [25,26]. This work uses the multiquadric (MQ) function proposed initially by Hardy [48]. Other functions were also used in an initial phase, however the best results were obtained with the MQ. The form of the MQ-RBF is

$$R(r_{Ii}) = (r_{Ii}^2 + c^2)^p, \tag{9}$$

where c and p are two parameters that need to be optimized. This is the major disadvantage of meshless methods using RBFs. The variation of these parameters can affect the performance of the RBFs.

In general, these two parameters can be obtained by numerical tests. In this work a patch test is used to calibrate the parameters. In order to ensure that the interpolation matrix of RBF is invertible, the polynomial basis added to the RBF cannot be arbitrary. It is common to add a low degree polynomial basis. In this work some distinct polynomial basis are experimented. In the 2D analysis

Null Basis – $\mathbf{x}^{\mathrm{T}} = \{x, y\}; \quad \mathbf{p}^{\mathrm{T}}(\mathbf{x}) = \{0\}; \quad m = 0,$ (10)

Constant Basis – $\mathbf{x}^{\mathrm{T}} = \{x, y\}; \quad \mathbf{p}^{\mathrm{T}}(\mathbf{x}) = \{1\}; \quad m = 1,$ (11)

Linear Basis – $\mathbf{x}^{\mathrm{T}} = \{x, y\}; \quad \mathbf{p}^{\mathrm{T}}(\mathbf{x}) = \{1, x, y\}; \quad m = 3,$

(12)

Quadratic Basis – $\mathbf{x}^{\mathrm{T}} = \{x, y\};$

$\mathbf{p}^{\mathrm{T}}(\mathbf{x}) = \{1, x, y, x^2, xy, y^2\}; \quad m = 6$ (13)

and for 3D analysis,

Null Basis – $\mathbf{x}^{\mathrm{T}} = \{x, y, z\}$; $\mathbf{p}^{\mathrm{T}}(\mathbf{x}) = \{0\}$; $m = 0$, $\qquad$ (14)

Constant Basis – $\mathbf{x}^{\mathrm{T}} = \{x, y, z\}$; $\mathbf{p}^{\mathrm{T}}(\mathbf{x}) = \{1\}$; $m = 1$, $\qquad$ (15)

Linear Basis – $\mathbf{x}^{\mathrm{T}} = \{x, y, z\}$; $\mathbf{p}^{\mathrm{T}}(\mathbf{x}) = \{1, x, y, z\}$; $m = 4$, $\quad$ (16)

Quadratic Basis – $\mathbf{x}^{\mathrm{T}} = \{x, y, z\}$;

$$\mathbf{p}^{\mathrm{T}}(\mathbf{x}) = \{1, x, y, z, x^2, xy, y^2, yz, z^2, zx\}; \ m = 10. \quad (17)$$

The polynomial basis has to satisfy an extra requirement in order to obtain an unique solution [49],

$$\sum_{i=1}^{n} p_j(\mathbf{x}_i) a_i(\mathbf{x}_i) = 0, \quad j = 1, 2, \ldots, m. \quad (18)$$

Therefore a new equation matrix can be written

$$\begin{Bmatrix} \mathbf{u}_s \\ 0 \end{Bmatrix} = \begin{bmatrix} \mathbf{R}_Q & \mathbf{P}_m \\ \mathbf{P}_m^{\mathrm{T}} & 0 \end{bmatrix} \begin{Bmatrix} \mathbf{a} \\ \mathbf{b} \end{Bmatrix} = \mathbf{G} \begin{Bmatrix} \mathbf{a} \\ \mathbf{b} \end{Bmatrix}, \quad (19)$$

where

$$\mathbf{u}_s = \{u_1, u_2, \ldots, u_n\}^{\mathrm{T}} \quad (20)$$

$$\mathbf{R}_Q = \begin{bmatrix} R(r_{11}) & R(r_{21}) & .. & R(r_{1n}) \\ R(r_{21}) & R(r_{22}) & .. & R(r_{2n}) \\ \vdots & \vdots & & \vdots \\ R(r_{n1}) & R(r_{n2}) & .. & R(r_{nn}) \end{bmatrix} \quad (21)$$

and the constant polynomial basis is defined as

$$\mathbf{P}_m = \begin{bmatrix} 1 & 1 & \ldots & 1 \end{bmatrix}^{\mathrm{T}} \quad (22)$$

being the linear polynomial basis for the 2D problem represented as

$$\mathbf{P}_m = \begin{bmatrix} 1 & 1 & \ldots & 1 \\ x_1 & x_2 & \ldots & x_n \\ y_1 & y_2 & \ldots & y_n \end{bmatrix}^{\mathrm{T}} \quad (23)$$

and for the 3D problem as

$$\mathbf{P}_m = \begin{bmatrix} 1 & 1 & \ldots & 1 \\ x_1 & x_2 & \ldots & x_n \\ y_1 & y_2 & \ldots & y_n \\ z_1 & z_2 & \ldots & z_n \end{bmatrix}^{\mathrm{T}}. \quad (24)$$

It must be noted that the geometric matrix $\mathbf{G}$ is a symmetric matrix because the distance is directional independent, i.e., $R(r_{ij}) = R(r_{ji})$. By solving Eq. (19),

$$\begin{Bmatrix} \mathbf{a} \\ \mathbf{b} \end{Bmatrix} = \mathbf{G}^{-1} \begin{Bmatrix} \mathbf{u}_s \\ 0 \end{Bmatrix} \quad (25)$$

and by substituting on Eq. (7),

$$\mathbf{u}(\mathbf{x}_I) = \{\mathbf{R}^{\mathrm{T}}(\mathbf{x}_I), \mathbf{p}^{\mathrm{T}}(\mathbf{x}_I)\} \mathbf{G}^{-1} \begin{Bmatrix} \mathbf{u}_s \\ 0 \end{Bmatrix} = \varphi(\mathbf{x}_I) \mathbf{u}_s, \quad (26)$$

where $\varphi(\mathbf{x})$ is the shape function defined as

$$\varphi(\mathbf{x}_I) = \{\mathbf{R}^{\mathrm{T}}(\mathbf{x}_I), \mathbf{p}^{\mathrm{T}}(\mathbf{x}_I)\} \mathbf{G}^{-1}$$
$$= \{\varphi_1(\mathbf{x}_I), \varphi_2(\mathbf{x}_I), \ldots, \varphi_n(\mathbf{x}_I)\}. \quad (27)$$

The partial derivative of $\varphi(\mathbf{x})$ in order to a variable ξ is defined as

$$\varphi_{,\xi}(\mathbf{x}_I) = \{\mathbf{R}_{,\xi}^{\mathrm{T}}(\mathbf{x}_I), \mathbf{p}_{,\xi}^{\mathrm{T}}(\mathbf{x}_I)\} \mathbf{G}^{-1}. \quad (28)$$

The partial derivatives of the MQ-RBF in order to x, y and z are

$$\mathbf{R}_{,x}(r_{ij}) = 2p(r_{ij}^2 + c^2)^{p-1}(x_j - x_i), \quad (29)$$

$$\mathbf{R}_{,y}(r_{ij}) = 2p(r_{ij}^2 + c^2)^{p-1}(y_j - y_i), \quad (30)$$

$$\mathbf{R}_{,z}(r_{ij}) = 2p(r_{ij}^2 + c^2)^{p-1}(z_j - z_i). \quad (31)$$

Early works on the RPIM [25,26] sustain that these shapes functions possess the delta Kronecker property

$$\varphi_i(\mathbf{x}_j) = \delta_{ij} = \begin{cases} 1 (i = j) \\ 0 (i \neq j) \end{cases} \quad i, j = 1, \ldots, n \quad (32)$$

and also that the partition of unity is satisfied

$$\sum_{i=1}^{n} \varphi_i(\mathbf{x}_i) = 1. \quad (33)$$

An inconvenient property of the RPIMs shape functions is the lack of compatibility, which means that the shape functions can not ensure the global continuity because the support domain is local. As a consequence the field function approximation could be discontinuous when nodes enter or leave the moving support domain. The compatibility of the RPIMs shape functions is achieved using the conforming RPIM (CRPIM) [50]. Studies on CRPIM and RPIM have concluded that CRPIM can exactly pass the standard patch tests and the RPIM cannot [41,50]. However, for the problems considered in the studies, the RPIM was also convergent and lead to satisfactory results. At the same, the RPIM is simpler and much more efficient than the CRPIM [4,50].

4. Galerkin weak form

In this work the two-dimensional plane stress problem and the three-dimensional problem are studied. Consider the solid with a domain Ω bounded by Γ. The equilibrium equations are expressed by

$$\nabla \boldsymbol{\sigma} + \mathbf{b} = 0 \quad \text{in } \Omega \quad (34)$$

being ∇ the gradient, $\boldsymbol{\sigma}$ the stress tensor and $\mathbf{b}$ the body force vector. The boundary conditions are given by

$$\boldsymbol{\sigma} \mathbf{n} = \bar{\mathbf{t}} \text{ on the natural boundary } \Gamma_t,$$
$$\mathbf{u} = \bar{\mathbf{u}} \text{ on the essential boundary } \Gamma_u, \quad (35)$$

where $\bar{\mathbf{u}}$ is the prescribed displacement on the essential boundary Γ_u, $\bar{\mathbf{t}}$ is the traction on the natural boundary Γ_t and $\mathbf{n}$ is the unit outward normal to the boundary of domain Ω. Considering the above equation, the Galerkin weak form is presented by

$$\mathcal{L} = \int_{\Omega} \delta \boldsymbol{\varepsilon}^{\mathrm{T}} \boldsymbol{\sigma} \, \mathrm{d}\Omega - \int_{\Omega} \delta \mathbf{u}^{\mathrm{T}} b \, \mathrm{d}\Omega - \int_{\Gamma_t} \delta \mathbf{u}^{\mathrm{T}} \mathbf{t} \, \mathrm{d}\Gamma = 0, \quad (36)$$

where $\boldsymbol{\varepsilon}$ is the strain vector, defined as

$$\boldsymbol{\varepsilon} = \mathbf{L}\mathbf{u} \tag{37}$$

and $\boldsymbol{\sigma}$ is defined by

$$\boldsymbol{\sigma} = \mathbf{c}\boldsymbol{\varepsilon} = \mathbf{c}\mathbf{L}\mathbf{u}, \tag{38}$$

where $\mathbf{L}$ is the differential operator defined in Eq. (39) for 3D analysis and $\mathbf{c}$ is the material matrix, Eq. (40), for the Hooke's law, for instances

$$\mathbf{L} = \begin{bmatrix} \frac{\partial}{\partial x} & 0 & 0 & \frac{\partial}{\partial y} & 0 & \frac{\partial}{\partial z} \\ 0 & \frac{\partial}{\partial y} & 0 & \frac{\partial}{\partial x} & \frac{\partial}{\partial z} & 0 \\ 0 & 0 & \frac{\partial}{\partial z} & 0 & \frac{\partial}{\partial y} & \frac{\partial}{\partial x} \end{bmatrix}^{\mathrm{T}}, \tag{39}$$

$$\mathbf{c} = \frac{E}{1-v^2} \begin{bmatrix} 1 & v & v & 0 & 0 & 0 \\ v & 1 & v & 0 & 0 & 0 \\ v & v & 1 & 0 & 0 & 0 \\ 0 & 0 & 0 & (1-v)/2 & 0 & 0 \\ 0 & 0 & 0 & 0 & (1-v)/2 & 0 \\ 0 & 0 & 0 & 0 & 0 & (1-v)/2 \end{bmatrix}. \tag{40}$$

Substituting Eq. (37) in the first term of Eq. (36),

$$\int_\Omega \delta\boldsymbol{\varepsilon}^{\mathrm{T}}\boldsymbol{\sigma}\,\mathrm{d}\Omega = \int_\Omega \delta(\mathbf{L}\mathbf{u})^{\mathrm{T}}\mathbf{c}(\mathbf{L}\mathbf{u})\,\mathrm{d}\Omega. \tag{41}$$

And considering Eq. (26)

$$\mathbf{u} = \sum_I^n \varphi_I u_I, \tag{42}$$

where n is the number of nodes inside the influence-cell, the following expression can be written:

$$\mathbf{L}\mathbf{u} = \mathbf{L}\sum_I^n \varphi_I \mathbf{u}_I = \sum_I^n \mathbf{L}\varphi_I \mathbf{u}_I$$

$$= \sum_I^n \begin{bmatrix} \frac{\partial\varphi_I}{\partial x} & 0 & 0 & \frac{\partial\varphi_I}{\partial y} & 0 & \frac{\partial\varphi_I}{\partial z} \\ 0 & \frac{\partial\varphi_I}{\partial y} & 0 & \frac{\partial\varphi_I}{\partial x} & \frac{\partial\varphi_I}{\partial z} & 0 \\ 0 & 0 & \frac{\partial\varphi_I}{\partial z} & 0 & \frac{\partial\varphi_I}{\partial y} & \frac{\partial\varphi_I}{\partial x} \end{bmatrix}^{\mathrm{T}} \mathbf{u}_I = \sum_I^n \mathbf{B}_I \mathbf{u}_I. \tag{43}$$

Eq. (36), can be developed

$$\mathscr{L} = \sum_I^n \sum_J^n \delta\mathbf{u}_I \underbrace{\int_\Omega \mathbf{B}_I^{\mathrm{T}}\mathbf{c}\mathbf{B}_J\,\mathrm{d}\Omega}_{K_{IJ}} \mathbf{u}_J - \sum_I^n \delta\mathbf{u}_I^{\mathrm{T}} \underbrace{\int_\Omega \varphi_I^{\mathrm{T}}\mathbf{b}\,\mathrm{d}\Omega}_{f_I}$$

$$- \sum_I^n \delta\mathbf{u}_I^{\mathrm{T}} \underbrace{\int_{\Gamma_t} \varphi_I^{\mathrm{T}}\bar{\mathbf{t}}\,\mathrm{d}\Gamma}_{\bar{f}_I} = 0 \tag{44}$$

and can be presented as

$$\mathscr{L} = \delta\mathbf{U}^{\mathrm{T}}[\mathbf{K}\mathbf{U} - \mathbf{F}] = 0, \tag{45}$$

Table 1
Flow chart of the numerical implementation

1. Determine each node neighbours and construct the correspondent Voronoï cells
2. Construct the integration points based on the Voronoï cells
3. Set the influence-cells (first or second degree)
4. Loop over the integration points in order to integrate the Galerkin Weak form
   a. Determine the nodes that directly influence the specified integration point, based on the previously defined integration-cells
   b. Compute the shape functions and its derivatives for each integration point
   c. Evaluate stiffness and load at each integration point
   d. Assemble the contribution of the specified integration point in order to form the system of equations
5. Introduce essential and natural boundaries
6. Solve the algebraic system to obtain the nodal displacement
7. Evaluate strain and stress at each integration point

where $\mathbf{U}=\mathbf{u}$ and $\mathbf{F} = \mathbf{f} + \bar{\mathbf{f}}$. As so the linear system of equations can be represented in the following matrix form:

$$\mathbf{K}\mathbf{U} = \mathbf{F}. \tag{46}$$

The essential boundary conditions can be directly imposed in the stiffness matrix $\mathbf{K}$, as in the FEM, once the RPIM shape function possesses the delta Kronecker property. The numerical implementation is summarized in Table 1.

5. Numerical examples

Some numerical examples are presented in this section with the purpose of demonstrating the good behaviour of the NNRPIM concerning the accuracy and the convergence of the method. For the convergence studies presented, the medium displacement error is defined as

$$\mathscr{E} = \frac{1}{n} \sum_i^n \frac{\sqrt{(u_i - u_{i\mathrm{exact}})^2 + (v_i - v_{i\mathrm{exact}})^2 + (w_i - w_{i\mathrm{exact}})^2}}{\sqrt{u_{i\mathrm{exact}}^2 + v_{i\mathrm{exact}}^2 + w_{i\mathrm{exact}}^2}} \tag{47}$$

and the medium stress error, for example for the normal stress σ_{xx}, is given by

$$\mathscr{E}_{\sigma_{xx}} = \frac{1}{n_Q} \sum_i^{n_Q} \frac{|\sigma_{xxi} - \sigma_{xx\mathrm{exact}}|}{|\sigma_{xx\mathrm{exact}}|}, \tag{48}$$

where n is the number of nodes that discretize the domain problem and n_Q is the number of integration points. In this section is presented a patch test, which is used to obtain the optimal shape parameters c and p, and several well-known problems from solid mechanics are solved [51]. Two dimensional finite element analysis is used for comparison, which is the nine node finite element with a 3×3 Gaussian quadrature integration scheme [1,2]. In this work the shape parameter c is obtained with,

$$c = \gamma A_{\mathrm{G}}, \tag{49}$$

where γ is a parameter that must be determined and A_{G} is a geometric parameter dependent on the mesh discretization.

5.1. The patch test

The patch test [52] was originally designed to prove the convergence in non-conforming finite element formulation. Generally the test consists on the imposition of a known displacement field in the boundary of the patch. If the pre-scribed field is reproduced in the interior of the patch then the test is verified.

Although being a benchmark for the evaluation and validation of non-conforming elements, in the context of the meshless methods the relevance of the patch test, from the convergence point of view, is still an open issue.

In the present work it is reproduced the patch test of the RPIM [25] in order to clearly explain the major differences between the RPIM and the NNRPIM and to introduce the NNRPIM procedure for the analysis considering the patch test.

5.1.1. RPIM patch test

The RPIM uses influence domains as Fig. 7(a) indicates. In this work, for the RPIM, influence domains of dimension $dm_I = C_I \times h$ are used, where $C_I = 2.5$ and h is the quadratic norm of the maximum distance between neighbour nodes. These values are according with the ones used in [25,26]. The background integration mesh is independent of the node mesh and it is created with integration cells each one with a quadrature scheme of 3×3 Gauss points, as Fig. 7(b) and (c) indicate for irregular and regular node meshes respectively.

In order to obtain the optimized parameters γ and p, firstly the parameter p is fixed, $p = 1.0001$, and the parameter γ is varied between 10 and 10^{-4}. The shape parameter c is obtained with the expression $c = h \times \gamma$. Once γ is minimized the process is repeated, but now with the minimized parameter c, $c = h \times \gamma_{\min}$, and varying the parameter p, until a minimum p is obtained.

In RPIM the linear polynomial basis is used, $\mathbf{p}(\mathbf{x}) = \{1 \; x \; y\}$, and the RBF is the MQ. The displacement field imposed on the boundary is defined by

$$\begin{cases} u = 0.1 + 0.1x, \\ v = 0.1 + 0.1y \end{cases} \tag{50}$$

and the medium displacement error, $\mathscr{E}$, defined in Eq. (47) is calculated. The sum of the interior equivalent forces is given by

$$f_{\text{tot}} = \sum_I^{n_i} \mathbf{f}_I^{\text{eq}}, \tag{51}$$

where n_i is the number of nodes that do not belong to the essential boundary and $\mathbf{f}^{\text{eq}}$ is the equivalent force obtained by the expression

$$\mathbf{f}^{\text{eq}} = \int_\Omega \mathbf{B}^{\text{T}} \boldsymbol{\sigma} \, \mathrm{d}\Omega. \tag{52}$$

Two mesh types are used in this case, an irregular and a regular mesh, as Fig. 7(b) and (c) indicate. The patch has the dimensions of $1.0 \times 1.0 \text{ m}^2$ and the material properties are $E = 1.0$ GPa and $v = 0.3$.

In Fig. 8(a) the medium displacement error is presented, Eq. (47), together with the f_{tot} as a function of the variation of the value of the parameter γ. It is visible that $\mathscr{E}$ stabilizes for values $\gamma \leqslant 1.6$. The stabilization and the minimization of f_{tot} is obtained for lower values of γ, $\gamma \leqslant 0.5$.

The parameter value suggested in Ref. [26] is $c = 1.43$, which corresponds to $\gamma \cong 7.0$, and $p = 1.03$. It is visible in Fig. 8(a) that such values for the parameters conduct to a medium displacement error $\mathscr{E} \cong 4 \times 10^{-4}$ and it produces a high value for f_{tot}, $f_{\text{tot}} \cong 1.5 \times 10^2$, which is unacceptable.

This anomaly is explained with the effective lack of the delta Kronecker property on the RPIM shape functions for high values of γ. It is noted that the value of the shape parameter c determines the fundamental shape of the basis function, with small value of γ the resulting multiquadric radial basis function is cone-shaped and with increasing values of γ the peak of the multiquadric radial basis function becomes flat. As a consequence, the value of the shape parameter γ affects the precision and the accuracy of the multiquadrics interpolation scheme. The increase of the
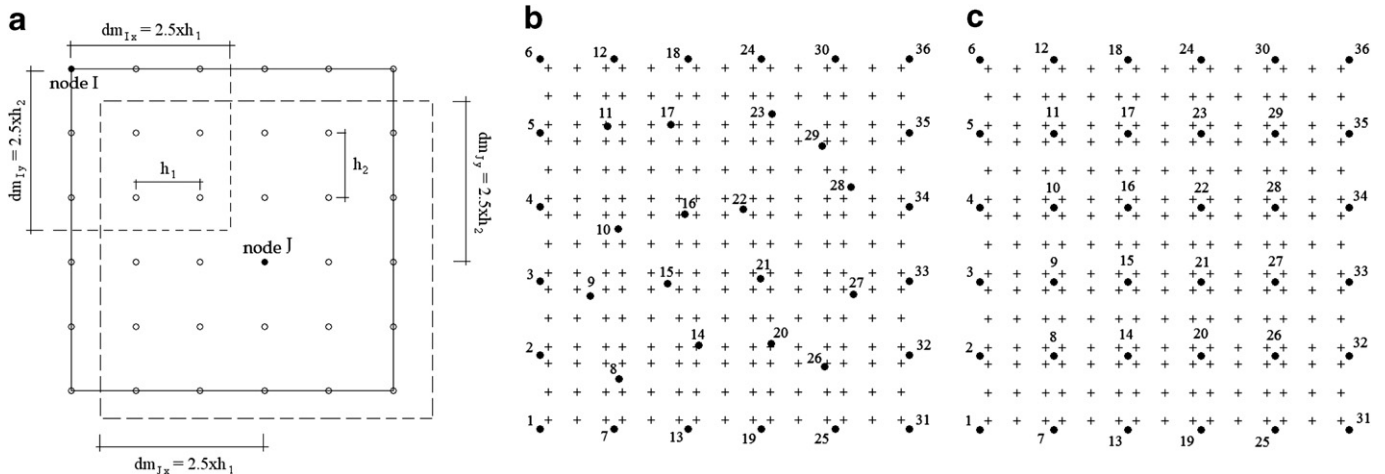

Fig. 7. (a) Construction examples of the influence domain, (b) irregular mesh and (c) regular mesh used to discretize the problem ("●" = nodes, "+S" = Gauss points).
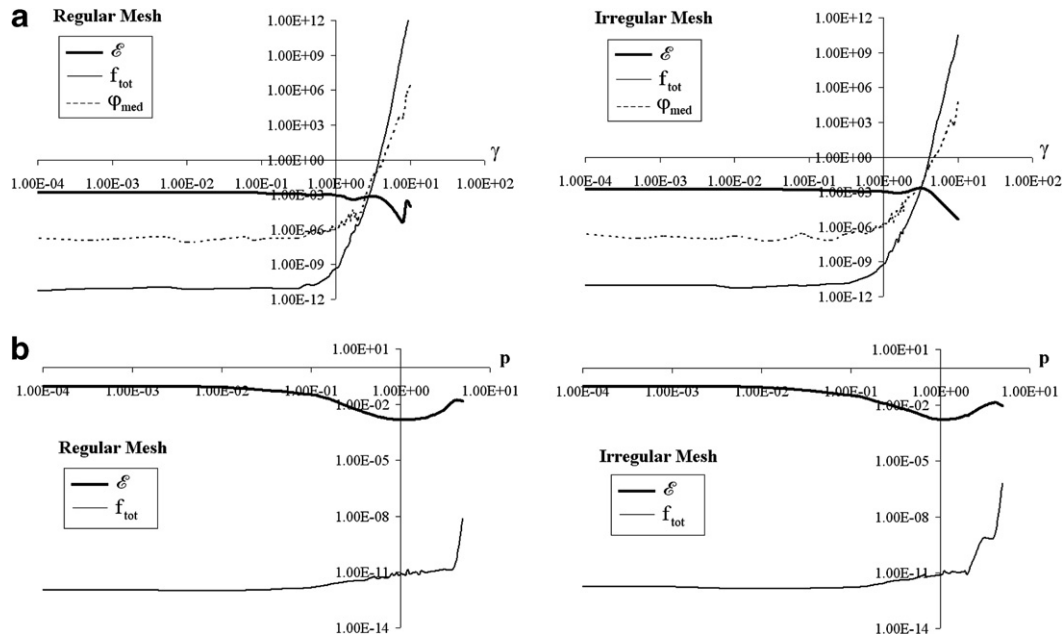
Fig. 8. (a) Shape parameter γ effects on the accuracy and (b) parameter p effects on the accuracy for the regular and irregular mesh. Logarithmic scales.

shape parameter implies a decrease of the approximation error. Nevertheless to adjust the shape parameter in order to improve the approximation accuracy, low values of γ, cause an ill-conditioned geometric **G** matrix or even the singularity of **G** [27].

It is now understandable that for high values of γ the shape function does not pass exactly on the nodes and to prove the statement, during previous analysis the shape function vector for the node 15, φ_{15}, was saved. The φ_{15} values on nodes 9, 14, 16 and 21 were used to calculate φ_{med},

$$\varphi_{med} = \frac{\varphi_{(15,9)} + \varphi_{(15,14)} + \varphi_{(15,16)} + \varphi_{(15,21)}}{4}. \tag{53}$$

It must be noted that these nodes are the closest nodes to node 15 and if φ_{15} has the delta Kronecker property, $\varphi_{(15,i)}$ should be zero for all $i \neq 15$, and consequently $\varphi_{med} = 0$. However it is visible in Fig. 8(a) that φ_{med} only stabilizes for $\gamma \leqslant 0.25$ and even for those values of γ, φ_{med} is different of zero, $\varphi_{med} \cong 10^{-7}$, which indicates the effective lack of the delta Kronecker property.

As in early works [25,26] the essential boundary conditions were directly imposed considering the existence of the delta Kronecker property, as in FEM. This is the reason why f_{tot} is always different from zero and even for $\gamma \leqslant 0.25$ is higher than the machine precision (10^{-16}). However, it is acceptable to consider, for $\gamma \leqslant 0.25$, that the RPIM shape functions possess the delta Kronecker property.

Considering $\gamma = 0.0001$ and the parameter p varying between 10 and 10^{-4} an optimal p is searched. All other considerations regarding material, geometric and boundary conditions remain the same. The integration scheme and

the nodal discretization are also similar to the previous analysis. The results are presented in Fig. 8(b).

It is visible in Fig. 8(b) that $p \cong 1$ is an optimal value once $\mathscr{E}$ and f_{tot} show a minimum for this value. However it was observed that p cannot be exactly equal to 1, or any other integer value, because it will generate a singular **G** matrix. Others authors [25,26] suggest the value $p = 1.03$. In this work the value used, in the RPIM, for parameter p is $p = 0.9999$.

5.1.2. NNRPIM patch test

In the NNRPIM the procedure to obtain the optimal shape parameters γ and p is similar to the procedure used for the RPIM. All considerations regarding the problem discretization, the material used, the geometry and boundary conditions remain the same as in previous example.

An optimization study was performed considering the NNRPIM with first degree influence-cell and afterwards considering the NNRPIM with the second degree influence-cell. In both formulations only the integration scheme of order 0 was used. The polynomial basis used in both formulations are the null basis, Eq. (10), the constant basis, Eq. (11), the linear basis, Eq. (12), and the quadratic basis, Eq. (13). Acronyms are used for a better understanding, the first two characters identify the degree of the influence cell, first degree = "v1" and second degree = "v2". The integration scheme order is identified by "ik", where k is the integration order. The polynomial basis is identified by "pm", where m is the number of monomials in the polynomial basis. For example, the formulation using a second degree influence-cell, an integration scheme of order 1 and a null polynomial basis is called: "v2i1p0".

In the NNRPIM the shape parameter c is obtained with the expression $c = \gamma \times \sqrt{A_{V_I}}$, where A_{V_I} is defined in Eq.

(3). The optimization procedure is equal to the previous patch test.

It was observed that the use of the quadratic polynomial basis on this formulation, v1i0p6, generates a **G** matrix singular, i.e. non invertible, and it was also observed that the v1i0p0 formulation fails the aim of producing an acceptable smooth stress field. Thus the study of these two formulations is abandoned.

In Table 2 the resulting $\mathscr{E}$ and f_{tot} for the obtained optimal shape parameters in the different formulations are presented.

As Table 2 shows the lowest medium displacement error $\mathscr{E}$, for irregular meshes, in the NNRPIM, is obtained with the v1i0p0, v1i0p1, v2i0p0 and the v2i0p1 formulation. This error is very close to the error obtained with the RPIM. It is noted as well that, generally the error obtained for regular meshes with NNRPIM is better than the error obtained with RPIM and that, for the v1i0p1 and v1i0p3 formulations, is very near the machine precision. It was also observed that the stress field of the v1i0p3, v2i0p3 and v2i0p6 formulation is highly irregular, therefore the NNRPIM study will continue only with the v1i0p0, v1i0p1, v2i0p0 and v2i0p1 formulations once the lowest medium displacement error is obtained with these formulations.

It is important to refer that the RPIM analysis is an optimized analysis because adequate shape parameters and proper integration schemes were applied. However in the case of the NNRPIM it was applied only the integra-tion scheme of order 0. Using the optimal shape parameters a study to obtain the optimal integration scheme is carried out.

The irregular mesh presented in Fig. 7(b) is used and the optimal shape parameters presented in Table 2 are applied to the RPIM and NNRPIM formulations. The problem is studied for various integration schemes for each formulation. The obtained medium displacement errors are presented in Fig. 9(a) and (b).

As Fig. 9 indicates, for the RPIM the integration scheme, 2×2 integration points in each integration cell seems to be sufficient, nevertheless in further problems the integration scheme will continue to be the 3×3 as Refs. [25,26] indicates.

In the NNRPIM with first degree influence-cell is visible that the integration schemes which conduct to more accurate results are the ones greater than order 1.

For the NNRPIM with second degree influence-cell formulation it is visible that an integration scheme of order 1 is sufficient.

The NNRPIM v1i2p0 formulation is abandoned once its computational cost is very high and it is less accurate than the NNRPIM v1i2p1 formulation.

The three-dimensional patch test was also studied, an unit cubic solid with a volume of $1.0 \times 1.0 \times 1.0 \, \text{m}^3$ and with the material properties $E = 1.0 \, \text{GPa}$ and $v = 0.3$ is submitted to an enforce displacement in all essential boundaries,

Table 2
$\mathscr{E}$ and f_{tot} obtained results for optimal shape parameters γ and p

|	Shape parameters		Regular mesh		Irregular mesh	
	γ	p	$\mathscr{E}$	f_{tot}	$\mathscr{E}$	f_{tot}
RPIM	0.0001	0.9999	1.51E−03	5.74E−12	1.67E−03	9.57E−12
v1i0p0	2	0.0001	8.00E−04	9.87E−11	5.10E−03	1.17E−10
v1i0p1	0.0001	0.9999	4.45E−11	4.88E−12	4.03E−03	6.56E−12
v1i0p3	0.0001	2.9999	1.09E−12	5.79E−12	8.89E−03	9.41E−12
v2i0p0	0.0001	0.9999	6.51E−04	9.63E−12	3.04E−03	8.77E−12
v2i0p1	0.0001	0.9999	4.59E−04	7.26E−12	2.67E−03	8.40E−12
v2i0p3	0.0001	0.9999	1.02E−02	2.52E−11	3.15E−02	3.30E−11
v2i0p6	0.0001	0.0001	6.50E−02	3.38E−12	8.98E−02	2.27E−12
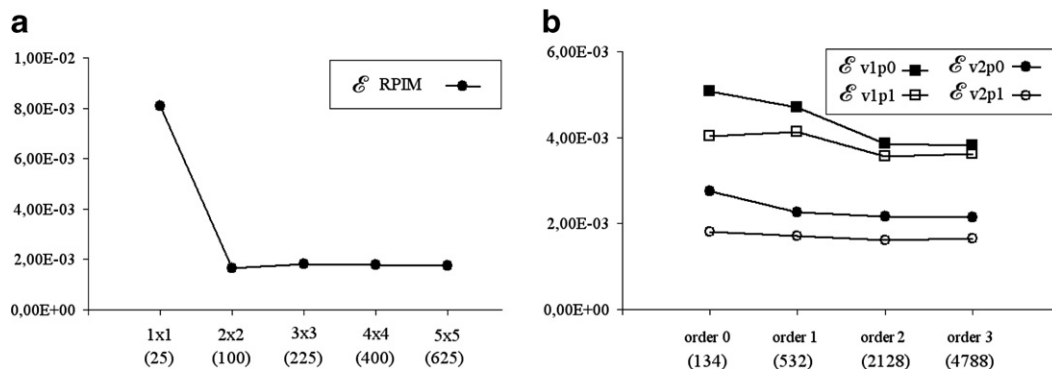
Fig. 9. Influence of the integration scheme on the accuracy for (a) RPIM and for (b) NNRPIM.

$$\begin{cases} u = 0.1 + 0.1x, \\ v = 0.1 + 0.2y, \\ w = 0.1 + 0.3z. \end{cases} \tag{54}$$

Once again the aim of the analysis is to obtain the optimal shape parameters, γ and p, for the 3D formulation. The solid was discretized with two distinct meshes, a regular mesh and an irregular mesh, both with $6 \times 6 \times 6$ nodes (216 nodes). The procedure is similar with the previous 2D patch-tests examples. The optimal shape parameters are presented in Table 3.

In the 3D study it was observed that the v1i0p0, v1i0p3, v2i0p3 and v2i0p6 NNRPIM formulations produce a stress field very irregular, which should be constant. In the table is also perceptible that the referred last three formulations compared with the others NNRPIM formulations present a higher medium displacement error. As so, in further examples using a 3D analysis the used NNRPIM formulations are the v1i0p1, v2i0p0 and the v2i0p1. Due to the significant computational cost, in this work, for the three-

Dimensional analysis the used integration scheme is the order 0.

To conclude this section Table 4 is presented, where the optimal parameters for the distinct formulation, used in further examples, are displayed.

5.2. The unit square plate under uniaxial stress

An unit square plate is submitted to an uniform uniaxial stress, $\sigma = 10$ kPa, in the x direction. The material, loading, geometry and boundary conditions are illustrated in Fig. 10(a). The analytical solution to this problem is given by

$$\begin{aligned} u &= \frac{\sigma}{E} \cdot \frac{x}{L}, \\ v &= -\frac{v\sigma}{E} \cdot \frac{y}{L}. \end{aligned} \tag{55}$$

The problem is discretized considering irregular and regular meshes. In Fig. 10(b) and (c) an irregular and a regular

Table 3
$\mathscr{E}$ and f_{tot} obtained results for optimal shape parameters γ and p in the 3D analysis

	Shape parameters		Regular mesh		Irregular mesh	
	γ	p	$\mathscr{E}$	f_{tot}	$\mathscr{E}$	f_{tot}
v1i0p0	0.0001	0.9999	7.66E−04	2.26E−14	1.65E−02	1.36E−10
v1i0p1	0.0001	0.9999	1.75E−03	3.18E−14	1.37E−02	4.33E−10
v1i0p3	0.0001	0.9999	1.60E−02	2.60E−13	3.41E−02	4.02E−10
v2i0p0	0.0001	0.9999	3.32E−03	6.61E−14	8.00E−03	3.69E−10
v2i0p1	0.0001	0.9999	3.20E−03	7.16E−14	7.30E−03	2.89E−09
v2i0p3	0.0001	0.9999	3.31E−02	4.41E−13	4.61E−02	6.39E−08
v2i0p6	0.0001	0.9999	5.31E−02	9.20E−13	5.68E−02	4.06E−09

Table 4
Obtained optimal parameter for the RPIM and NNRPIM formulations

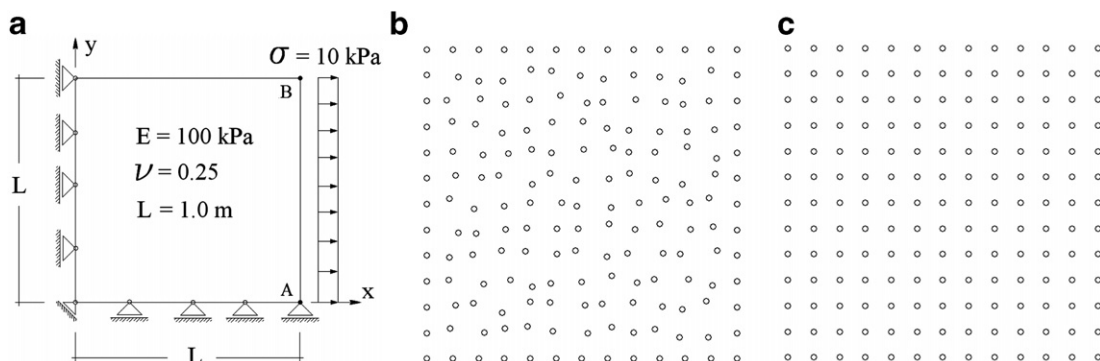| Parameters	RPIM 2D	v1p1 2D	v2p0 2D	v2p1 2D	v1p1 3D	v2p0 3D	v2p1 3D
γ	0.0001	0.0001	0.0001	0.0001	0.0001	0.0001	0.0001
p	0.9999	0.9999	0.9999	0.9999	0.9999	0.9999	0.9999
Integration scheme	3×3	Order 2	Order 1	Order 1	Order 0	Order 0	Order 0

Fig. 10. (a) Considered material and geometric conditions of the unit square plate problem, (b) irregular 169 node mesh and (c) regular 169 node mesh.

mesh of 169 nodes are presented, which will be used in the problem analysis.

In Fig. 11 is presented the convergence study for the displacement values of points A and B, represented in Fig. 10. Fig. 11 shows that the NNRPIM formulation convergence rate in comparison with the RPIM formulation is higher and the converged result is very near the exact solution ($u_A = 0.1$, $u_B = 0.1$ and $v_B = 0.025$).

Fig. 12(a) and (b) show the results, for the irregular and regular meshes respectively, of the convergence study for the medium displacement error, Eq. (47). It is visible that using an irregular mesh the NNRPIM v1i2p1 formulation presents a high medium displacement error and when the regular mesh is considered the error is very low (10^{-4}). Fig. 12 enforces the former statement, the NNRPIM for-

mulations have a high convergence rate in comparison with the RPIM formulation.

The present problem should generate a constant stress field,

$$\boldsymbol{\sigma} = \{\ \sigma_{xx} \quad \sigma_{yy} \quad \sigma_{xy}\ \} = \{\ \sigma \quad 0 \quad 0\ \}, \qquad (56)$$

where $\sigma = 10$ kPa. Thus the medium stress error is calculated by using Eq. (48). In Fig. 12(c) and (d) the results for the irregular and regular meshes are shown.

It is visible in Fig. 12(d) that the NNRPIM formulations for regular meshes converge faster to the exact solution than the RPIM formulation. It is also visible in Fig. 12(c) that when an irregular mesh is used the v2i1p0 and the v2i1p1 are the only NNRPIM formula-
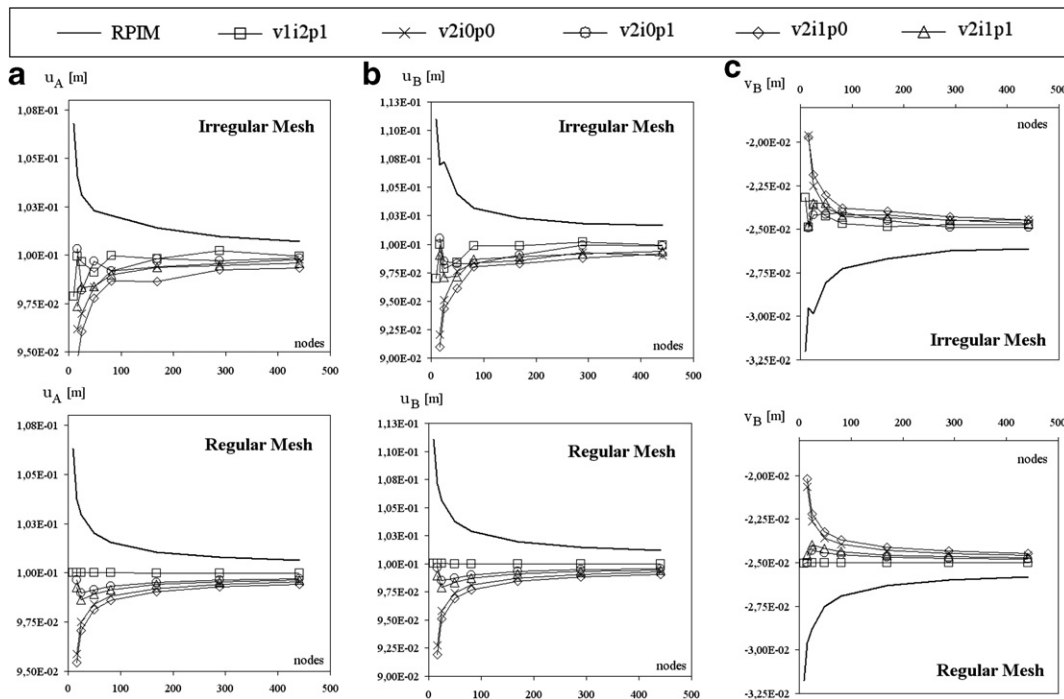

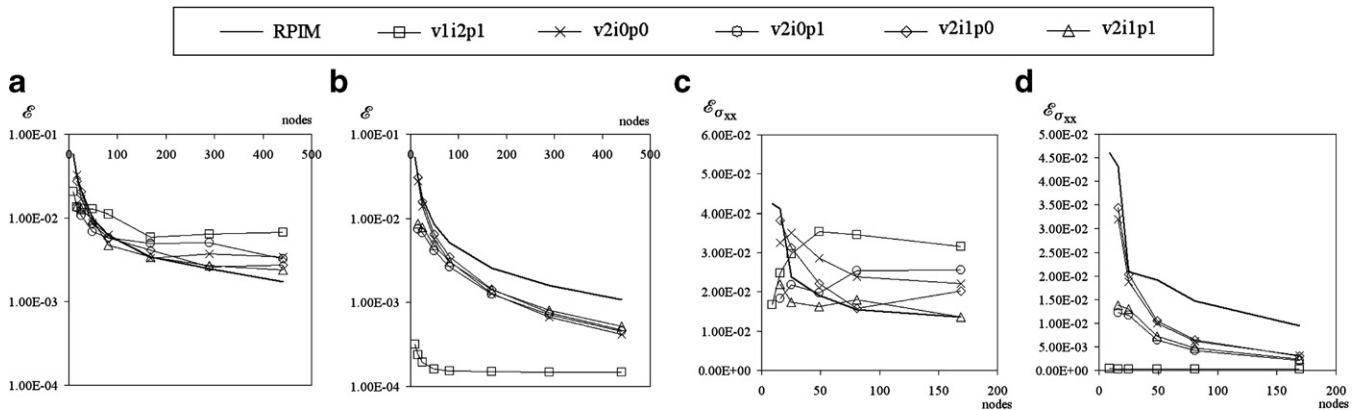
Fig. 11. Displacement values for the interest points.

Fig. 12. Medium displacement error in relation to the number of nodes obtained with the (a) irregular mesh and with the (b) regular mesh, yy-axis in logarithmic scale. Medium stress error, in relation to the number of nodes, obtained with the (c) irregular mesh and with the (d) regular mesh.

tions that produce similar results with the RPIM formulation.

Another interesting point is the computational effort of the method. Fig. 13 presents the medium displacement errors in relation to the time spent in the analysis.

As Fig. 13 shows, using a regular mesh, the NNRPIM, with the lower integration scheme, presents a lower computational cost when compared with the RPIM and that the time spent in the analysis is even lower when irregular meshes are considered, which is explained with the lower number of nodes in each influence-cell in the case of the irregular meshes. It must be noted that, the computational cost of the regular meshes is about the double of the irregular meshes. The NNRPIM with the v1i2p1 formulation presents a very high computational cost, which is explained by the number of integration nodes generated with the second degree integration scheme.

In the second degree influence-cell NNRPIM formulations no significant differences are observed using an integration scheme of order 0 or of order 1. As so, in further examples only the v2i0p0 and the v2i0p1 are used once these formulations present a much lower computational cost.

5.3. The cantilever beam

The cantilever beam problem is also used to study the accuracy of the NNRPIM. The schematic illustration of the problem is presented in Fig. 14(a). The exact solution for the displacement field of the 2D problem is given by,

$$u = -\frac{Py}{6EI}\left[(2L-x)3x + (2+v)\left(y^2 - \frac{D^2}{4}\right)\right],$$

$$v = \frac{P}{6EI}\left[x^2(3L-x) + 3v(L-x)y^2 + \frac{4+5v}{4}D^2x\right],$$

(57)

where I is the moment of inertia, $I = D^3/12$. The stress field for the same dimensional problem is

$$\sigma_{xx} = -\frac{P(L-x)y}{I},$$

$$\sigma_{yy} = 0,$$

$$\sigma_{xy} = \frac{P}{2I}\left(\frac{D^2}{4} - y^2\right).$$

(58)

The problem is solved considering the 2D plane stress analysis and the three-dimensional analysis. The domain is discretized in irregular and regular meshes. In Fig. 14(b) and (c) is given an example of a regular and an irregular and mesh of 231 nodes used in the 2D problem analysis. In Fig. 14(d) and (e) is given an example of a regular and an irregular mesh of 637 nodes used in the 3D problem analysis.

In order to compare the obtained results between the 3D analysis and the 2D analysis, in the following diagrams
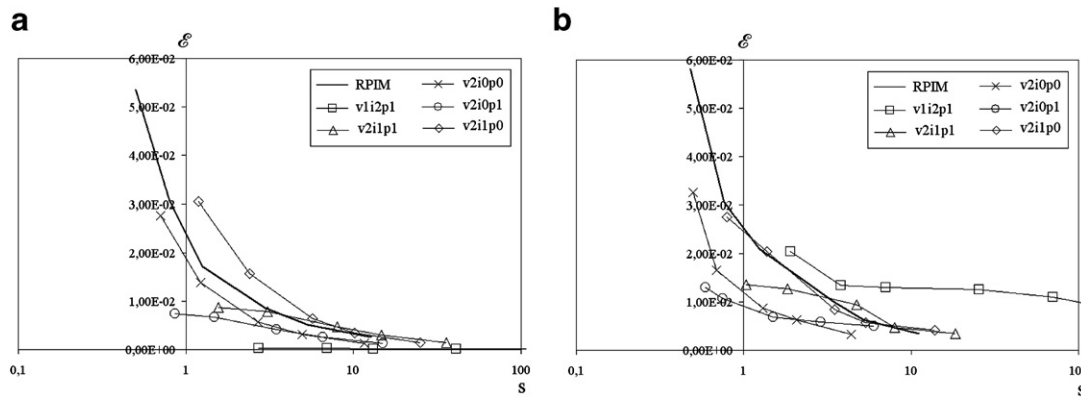

Fig. 13. Medium displacement error, in relation to the computational cost, in a logarithmic scale, obtained with the (a) regular mesh and with the (b) irregular mesh.
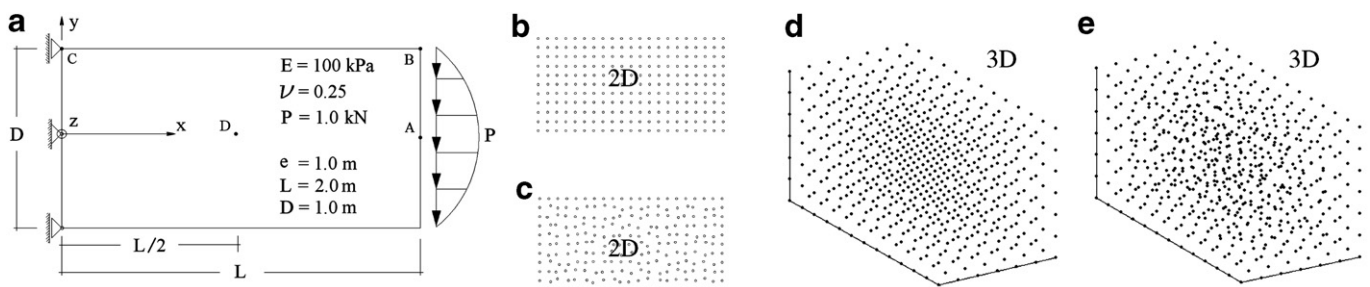

Fig. 14. (a) Considered material and geometric conditions of the cantilever beam problem, (b) 2D Regular 231 node mesh, (c) 2D Irregular 231 node mesh, (d) 3D Regular 637 node mesh and (e) 3D Irregular 637 node mesh.

only the number of nodes of the face Oxy of the 3D mesh are represented.

In Fig. 15 are shown the medium displacement errors, $\mathscr{E}$, and the medium stress errors, $\mathscr{E}_{\sigma_{xx}}$ and $\mathscr{E}_{\sigma_{xy}}$. These results were obtained using irregular meshes and regular meshes. In Fig. 16 are presented the displacement values of interest points A and B, in relation to number of nodes used to discretize the problem, for the irregular and the regular meshes.

It is visible in Figs. 15 and 16 that once again, within the NNRPIM formulation, when an irregular mesh is considered the v1i2p1 generates the worst result. It is also visible

in Fig. 15 that the NNRPIM formulation has a faster convergence to the exact solution when compared with the RPIM formulation. In general the medium errors are lower when second degree influence-cells are used, in the 2D and in the 3D analysis. The results for the 3D analysis seem to be worse than the ones produced by the 2D analysis. This discrepancy is manly due to the difficulty of comparing the different discretization of the problem for the distinct analysis, 2D and 3D.

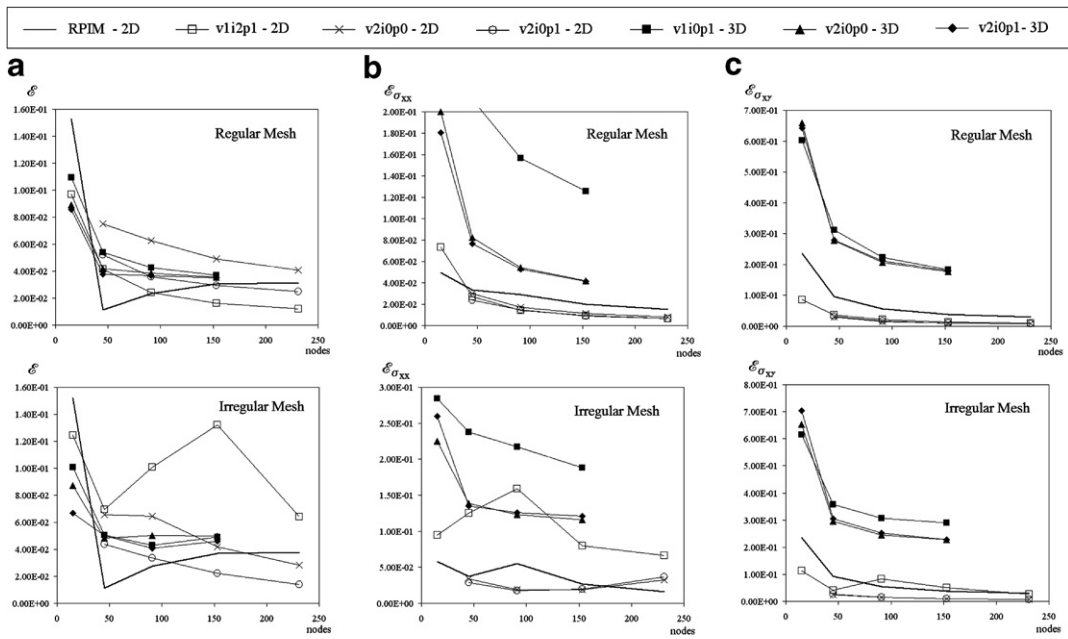In Fig. 16, for the 2D analysis, it is visible that the NNRPIM formulations converge with more accuracy

Fig. 15. (a)Medium displacement error,$\mathscr{E}$, (b) medium stress error, $\mathscr{E}_{\sigma_{xx}}$, (c) medium stress error, $\mathscr{E}_{\sigma_{xy}}$.
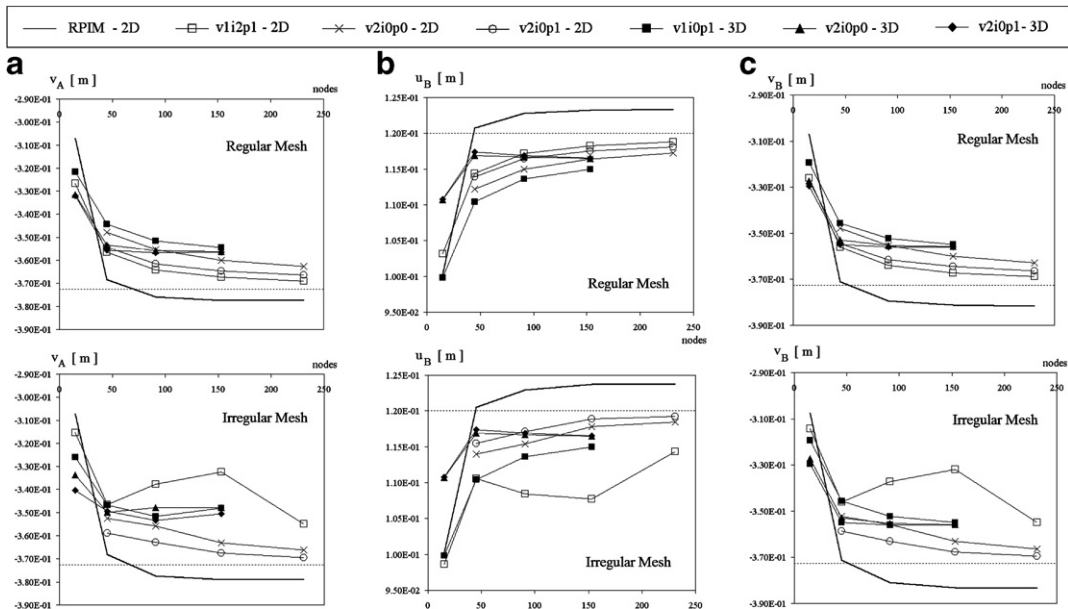

Fig. 16. Displacement values obtained with irregular and regular meshes in interest points A and B.

to the exact solution when compared with the RPIM formulation.

It was observed that the horizontal component of the displacement on interest point A on neutral axis, u_A, for all the NNRPIM formulations is equal to the machine precision, 10^{-16}, and for the RPIM formulation is about 10^{-6}.

In Fig. 17 the normal stress σ_{xx} of the interest point C and the shear stress σ_{xy} of the interest point D, for the regular and the irregular mesh, are shown.

The results obtained for the shear stress σ_{xy} in the interest point D show a good concordance between the two formulations. However the results for the normal stress σ_{xx} in the interest point C show that all NNRPIM formulation are less accurate when compared with the RPIM formulation. Such results can be explained by the fact that the integration point where the stress is obtained for the RPIM is always much close to point C compared with the closest integration point in the NNRPIM. It must be noted as

well, that for the stress result for the solution obtained with the 3D analysis approaches the solution obtained with a 2D analysis.

5.4. The infinite plate with a circular hole

An infinite plate with a circular hole is considered, due to the existing symmetry only the upper right quadrant of the plate is analysed, as represented in Fig. 18(a). The traction illustrated on the natural boundary conditions is given by the exact solution,

$$\begin{aligned}
\sigma_{xx} &= 1 - \frac{a^2}{r^2}\left(\frac{3}{2}\cos(2\theta) + \cos(4\theta)\right) + \frac{3a^4}{2r^4}\cos(4\theta), \\
\sigma_{yy} &= -\frac{a^2}{r^2}\left(\frac{1}{2}\cos(2\theta) - \cos(4\theta)\right) - \frac{3a^4}{2r^4}\cos(4\theta), \\
\sigma_{xy} &= -\frac{a^2}{r^2}\left(\frac{1}{2}\sin(2\theta) + \sin(4\theta)\right) + \frac{3a^4}{2r^4}\sin(4\theta).
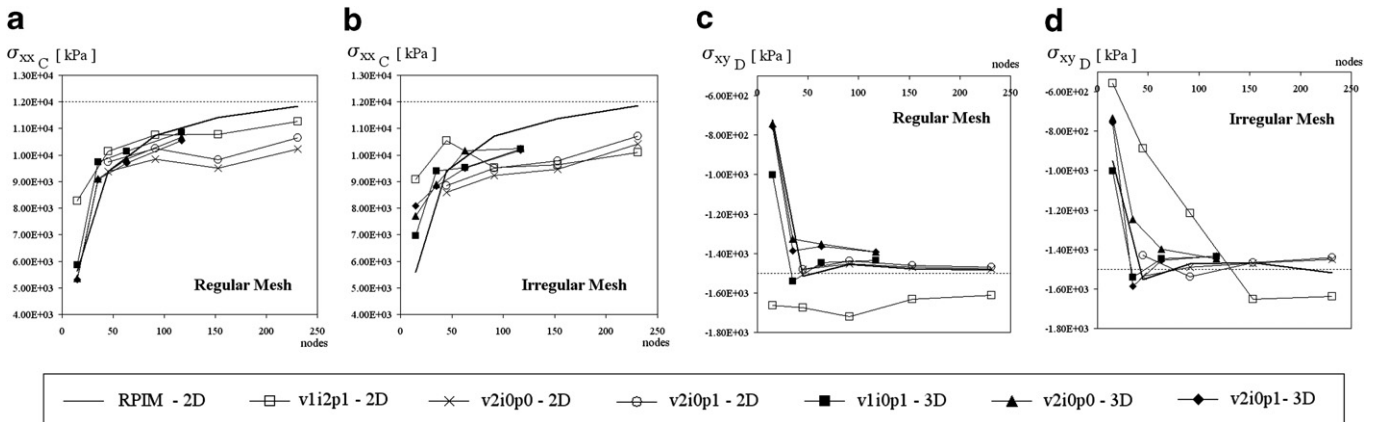\end{aligned} \tag{59}$$

Fig. 17. Stress values on the interest points C and D for irregular meshes and for regular meshes.
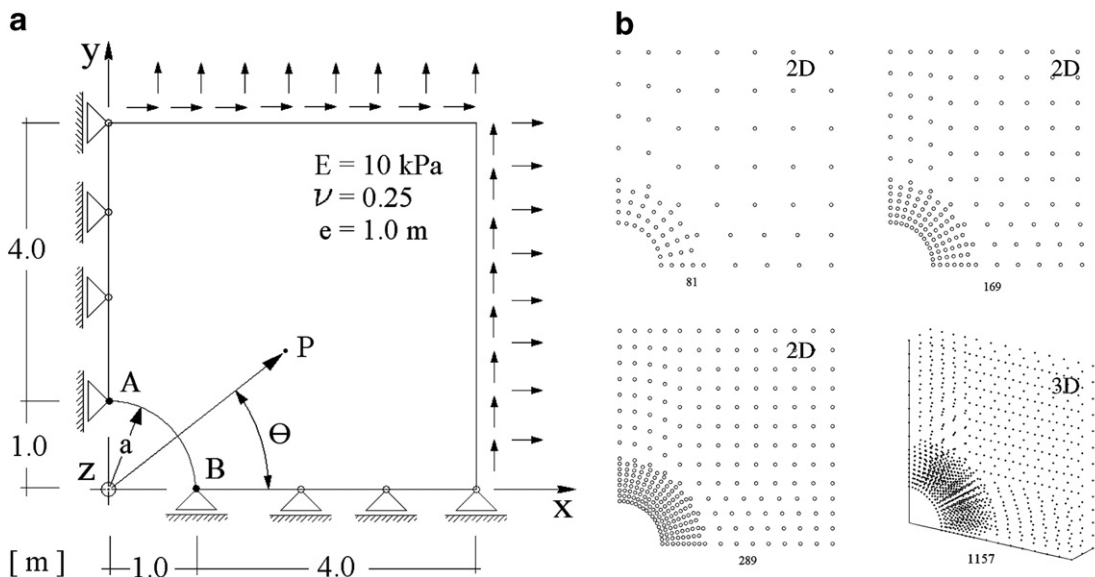

Fig. 18. (a) Material and geometrical characteristics and boundary and load conditions of the plate with a circular hole and (b) examples of the regular nodal discretization for the plate with a circular hole.

In this problem only regular meshes are used, and examples are presented in Fig. 18(b).

In Fig. 19(a) and (b) are presented the displacement values on interest points A and B, indicated in Fig. 18. It is visible that the NNRPIM converges with a higher rate when compared with the FEM and the RPIM. It is also seen that the performance of the NNRPIM formulation is not affected by the used integration scheme, once both integration schemes produce similar results. It is visible that the NNRPIM 3D analysis produces results very close to the FEM 2D analysis.

In Fig. 20(a)–(c) are presented the medium stress errors, $\mathscr{E}_{\sigma_{xx}}$, $\mathscr{E}_{\sigma_{yy}}$ and $\mathscr{E}_{\sigma_{xy}}$, and in Fig. 20(d) and (e) are presented the obtained normal stress σ_{xx} and σ_{yy}, respectively for interest points A and B.

In Fig. 20 it can be seen that the NNRPIM has, once again, a convergence rate considerably higher than the FEM or the RPIM. It is also observed that the stress field produced by the NNRPIM is very smooth. Once again the results obtained with the NNRPIM 3D analysis approaches the FEM solution.
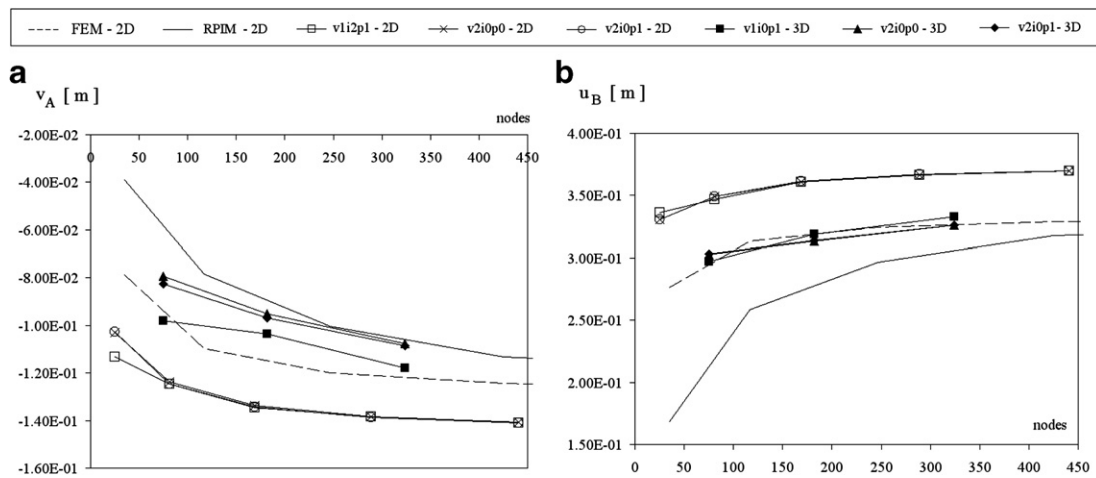

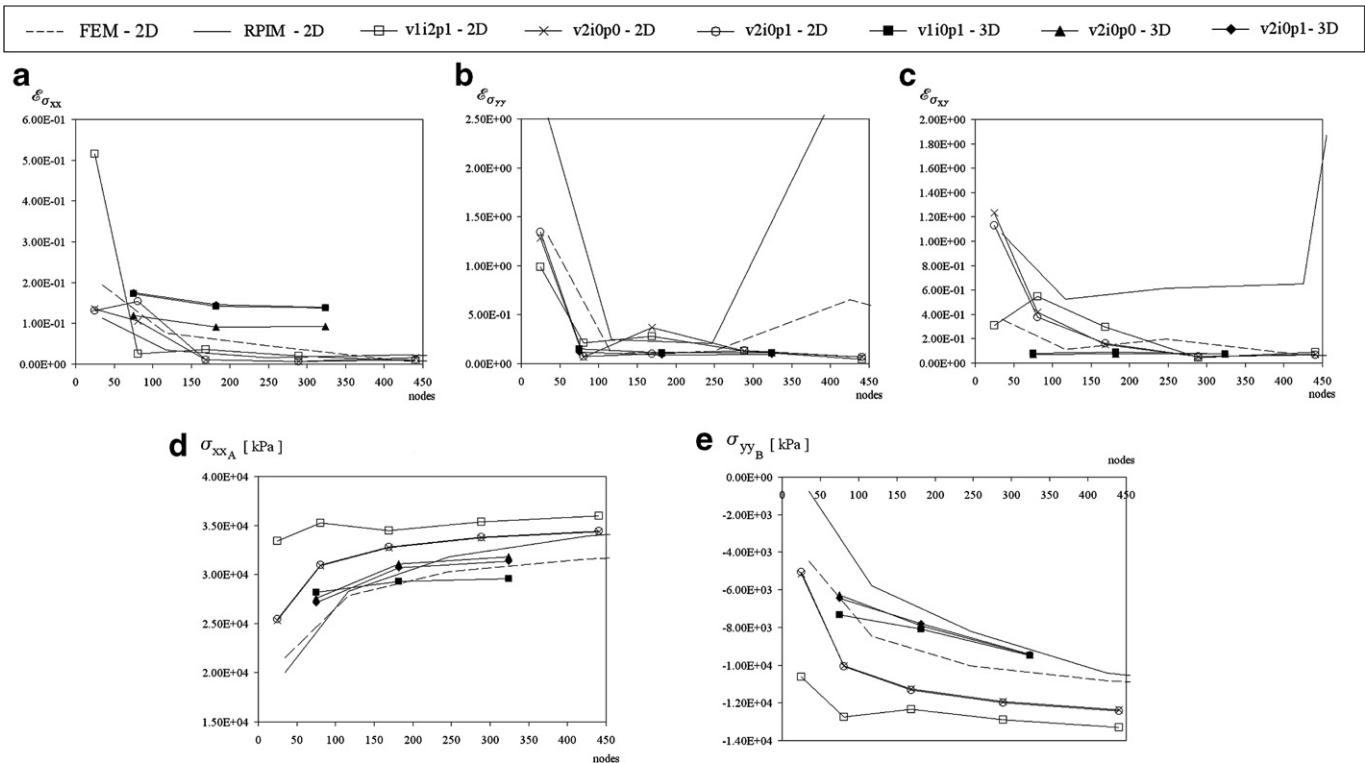Fig. 19. Displacement values in interest points (b) A and (c) B.

Fig. 20. Medium stress error (a) $\mathscr{E}_{\sigma_{xx}}$, (b) $\mathscr{E}_{\sigma_{yy}}$ and (c) $\mathscr{E}_{\sigma_{xy}}$. Stress values in interest points (d) A and (e) B.
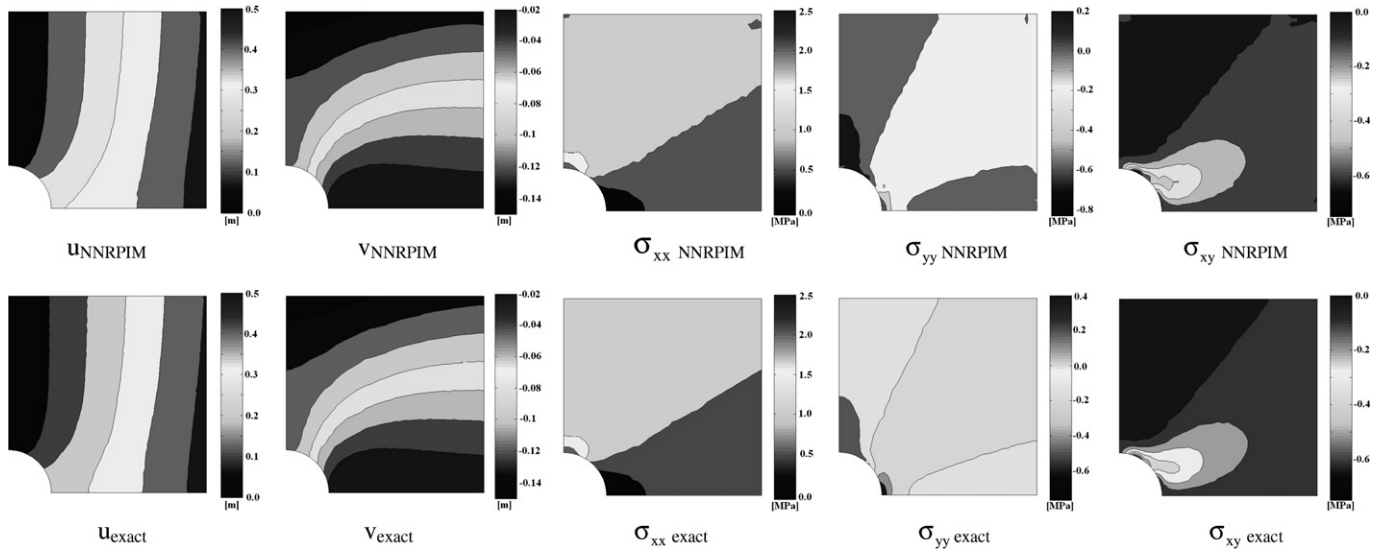
Fig. 21. Displacement field and the stress distribution obtained with the NNRPIM and with the exact solution.

In Fig. 21 is presented the displacement field and the stress distribution obtained with the NNRPIM and with the exact solution.

The results obtained show an almost perfect similarity between the NNRPIM solution and the exact solution and that the NNRPIM is capable of producing smooth displacement and smooth stress fields.

6. Conclusions

In this work an improved radial point interpolation method is presented, using the multiquadric radial basis function, with the Voronoï tessellation and the Delaunay triangulation, in order to obtain the nodal connectivity and the integration background mesh respectively. To form NNRPIM the interpolation functions are applied to the Galerkin weak form of solid mechanics. The capability of reproducing a displacement field is tested for distinct NNRPIM formulations and the optimal shape parameters to 2D and 3D problems are obtained. Considering the optimal shape parameters convergence and accuracy studies are performed for some classic problems of the solid mechanics. The most relevant conclusions of this work can be summarized as follows:

1. It is reasonable to considerer that the radial point interpolation methods shape functions respect the delta Kronecker function but only for small values of the shape parameter γ, $\gamma \leqslant 0.25$. As so the shape functions obtained have the delta Kronecker property, thus overcoming the disadvantage on the imposition of the essential and natural boundary conditions so well-known in element-free methods based on MLS approximation.

2. In the presented examples it is clear that the most efficient NNRPIM formulation is the one that uses the second degree influence-cell. In the patch tests presented is clear that the appropriate integration scheme is the integration scheme of order 1, however the examples solved show that

in fact there is no significant difference between the integration scheme of order 0 and of order 1. Thus the integration scheme of order 0 is preferable once it has a lower computational cost. The results show that there is no significant difference when no polynomial basis is used or when a constant polynomial basis is used. However stress distributions are more smooth and accurate in the case of the constant polynomial basis.

3. The optimal shape parameters obtained in this initial study for the NNRPIM formulations with second degree influence-cell are $\gamma \leqslant 0.0001$ and $p = 0.9999$.

4. It was shown that the computational effort of the NNRPIM is low, comparable with the RPIM. However as the RPIMs use more nodes in the interpolation the computational efficiency is lower when compared with the FEM.

5. Comparing the NNRPIM with the nine node FEM in a problem with convex boundaries it is clear that the NNRPIM has a higher accuracy and convergence rate.

6. In the 3D analysis the NNRPIM results show a good behaviour, very close to the results obtained with FEM. Although the NNRPIM is computationally less efficient then the FEM.

References

[1] K.J. Bathe, Finite Element Procedures, Prentice-Hall, Englewood Cliffs, NJ, 1996.
[2] O.C. Zienkiewicz, The Finite Element Method, fourth ed., McGraw-Hill, 1989.

[3] T. Belytschko, Y. Krongauz, D. Organ, M. Fleming, P. Krysl, Meshless methods: an overview and recent developments, Comput. Methods Appl. Mech. Engrg. 139 (1) (1996) 3–47.

[4] Y.T. Gu, Meshfree methods and their comparisons, Int. J. Comput. Methods 2 (4) (2005) 477–515.

[5] B. Nayroles, G. Touzot, P. Villon, Generalizing the finite element method: diffuse approximation and diffuse elements, Comput. Mech. 10 (1992) 307–318.

[6] P. Lancaster, K. Salkauskas, Surfaces generation by moving least squares methods, Math. Comput. 37 (1981) 141–158.

[7] T. Belytschko, Y.Y. Lu, L. Gu, Element-free Galerkin method, Int. J. Numer. Methods Engrg. 37 (1994) 229–256.

[8] J. Dolbow, T. Belytschko, An introduction to programming the meshless element free Galerkin method, Arch. Comput. Mech. 5 (3) (1998) 207–241.

[9] Y. Lu, T. Belytschko, L. Gu, A new implementation of the element free Galerkin method, Comput. Methods Appl. Mech. Engrg. 113 (1994) 397–414.

[10] J.J. Monaghan, Smoothed particle hydrodynamics: theory and applications to non-spherical stars, Mon. Notices Astronom. Soc. 181 (1977) 375–389.

[11] W.K. Liu, S. Jun, Y.F. Zhang, Reproducing kernel particle methods, Int. J. Numer. Methods Fluids 20 (6) (1995) 1081–1106.

[12] S.N. Atluri, T. Zhu, A new meshless local Petrov–Galerkin (MLPG) approach in computational mechanics, Comput. Mech. 22 (2) (1998) 117–127.

[13] E. Oñate, S. Idelsohn, O.C. Zienkiewicz, R.L. Taylor, A finite point method in computational mechanics – applications to convective transport and fluid flow, Int. J. Numer. Methods Engrg. 39 (1996) 3839–3866.

[14] K.J. Bathe, S. De, Towards an efficient meshless computational technique: the method of finite spheres, Engrg. Comput. 18 (2001) 170–192.

[15] G.R. Liu, Y.T. Gu, A point interpolation method for two-dimensional solids, Int. J. Numer. Methods Engrg. 50 (2001) 937–951.

[16] J.G. Wang, G.R. Liu, Y.G. Wu, A point interpolation method for simulating dissipation process of consolidation, Comput. Methods Appl. Mech. Engrg. 190 (2001) 5907–5922.

[17] G.R. Liu, A point assembly method for stress analysis for two-dimensional solids, Int. J. Solid Struct. 39 (2002) 261–276.

[18] L. Traversoni, Natural neighbour finite elements, Int. Conf. Hydraulic Engrg. Software, Hydrosoft Proc., Comput. Mech. Pub. 2 (1994) 291–297.

[19] N. Sukumar, B. Moran, A. Yu Semenov, V.V. Belikov, Natural neighbour Galerkin methods, Int. J. Numer. Methods Engrg. 50 (1) (2001) 1–27.

[20] J. Braun, M. Sambridge, A numerical method for solving partial differential equations on highly irregular evolving grids, Nature 376 (1995) 655–660.

[21] N. Sukumar, B. Moran, T. Belytschko, The natural element method in solid mechanics, Int. J. Numer. Methods Engrg. 43 (5) (1998) 839–887.

[22] E. Cueto, M. Doblaré, L. Gracia, Imposing essential boundary conditions in the natural element method by means of density-scaled-shapes, Int. J. Numer. Methods Engrg. 49 (4) (2000) 519–546.

[23] E. Cueto, N. Sukumar, B. Calvo, J. Cegoñino, M. Doblaré, Overview and recent advances in the natural neighbour Galerkin method, Arch. Comput. Methods Engrg. 10 (4) (2003) 307–387.

[24] R. Sergio, S. Idelsohn, E. Oñate, N. Calvo, F. Del Pin, The meshless finite element method, Int. J. Numer. Methods Engrg. 58 (6) (2003) 893–912.

[25] J.G. Wang, G.R. Liu, A point interpolation meshless method based on radial basis functions, Int. J. Numer. Methods Engrg. 54 (2002) 1623–1648.

[26] J.G. Wang, G.R. Liu, On the optimal shape parameters of radial basis functions used for 2-D meshless methods, Comput. Methods Appl. Mech. Engrg. 191 (2002) 2611–2630.

[27] E.J. Kansa, A scattered data approximation scheme with applications to computational fluid-dynamics – I and II, Comput. Math. Appl. 19 (1990) 127–161.

[28] G.R. Liu, B.T. Bernard, L. Chun, A stabilized least-squares radial point collocation method (LS-RPCM) for adaptive analysis, Comput. Methods Appl. Mech. Engrg. 195 (2006) 4843–4861.

[29] G.R. Liu, G.Y. Zhang, Y.T. Gu, Y.Y. Wang, A meshfree radial point interpolation method (RPIM) for three-dimensional solids, Comput. Mech. 36 (6) (2005) 421–430.

[30] G.R. Liu, K.Y. Dai, K.M. Lim, Y.T. Gu, A point interpolation meshfree method for static and frequency analysis of two-dimensional piezoelectric structures, Comput. Mech. 29 (6) (2002) 510–519.

[31] G.R. Liu, K.Y. Dai, K.M. Lim, Y.T. Gu, A radial point interpolation method for simulation of two-dimensional piezoelectric structures, Smart Mater. Struct. 12 (2003) 171–180.

[32] X.L. Chen, K.M. Liew, Buckling of rectangular functionally graded material plates subjected to nonlinearly distributed in-plane edge loads, Smart Mater. Struct. 13 (2004) 1430–1437.

[33] K.Y. Dai, G.R. Liu, K.M. Lim, A meshfree method for static and free vibrations analysis of shear deformable laminated composite plates, J. Sound Vib. 269 (3–5) (2004) 633–652.

[34] K.M. Liew, X.L. Chen, Mesh-free radial point interpolation method for the buckling analysis of Mindlin plates subjected to in-plane point loads, Int. J. Numer. Methods Engrg. 60 (2004) 1861–1877.

[35] K.M. Liew, X.L. Chen, Buckling of rectangular Mindlin plates subjected to partial in-plane edge loads using the radial point interpolation method, Int. J. Solids Struct. 41 (2004) 1677–1695.

[36] K.M. Liew, X.L. Chen, J.N. Reddy, Mesh-free radial basis function method for buckling analysis of non-uniformly loaded arbitrarily, Comput. Methods Appl. Mech. Engrg. 193 (2004) 205–224.

[37] Y. Liu, Y.C. Hon, K.M. Liew, A meshfree Hermite-type radial point interpolation method for Kirchhoff plate problems, Int. J. Numer. Methods Engrg. 66 (2006) 1153–1178.

[38] R. Sibson, A brief description of natural neighbor interpolation, in: V. Barnett (Ed.), Interpreting Multivariate Data, Wiley, Chichester, 1981, pp. 21–36.

[39] G.M. Voronoï, Nouvelles applications des paramètres continus à la théorie des formes quadratiques. Deuxième Mémoire: Recherches sur les parallélloèdres primitifs, J. Reine Angew. Math. 134 (1908) 198–287.

[40] B. Delaunay, Sur la sphére vide. A la memoire de Georges Voronoï. Izv. Akad. Nauk SSSR, Otdelenie Matematicheskih i Estestvennyh Nauk 7 (1934) 793–800.

[41] G.R. Liu, Mesh Free Methods, Moving beyond the Finite Element Method, CRC Press, 2002.

[42] L. Dinis, J. Belinha. Analysis of 2D problems resorting to a new meshless method, in: III European Conference on Computational Mechanics – Solids, Structures and Coupled Problems in Engineering, 2006, Lisbon, LNEC, 5–9 June.

[43] L. Dinis, J. Belinha. A numerical comparison of distinct meshless methods for the analysis of composite laminates, in: III European Conference on Computational Mechanics – Solids, Structures and Coupled Problems in Engineering, 2006, Lisbon, LNEC, 5–9 June.

[44] R. Sibson, A vector identity for the Dirichlet tesselation, Math. Proc. Cambridge Philos. Soc. 87 (1980) 151–155.

[45] C.L. Lawson, Software for C1 surface interpolation, in: J.R. Rice (Ed.), Mathematical Software III, vol. 3, Academic Press, New York, NY, 1977.

[46] D.F. Watson, Contouring: A Guide to the Analysis and Display of Spatial Data, Pergamon Press, Oxford, 1992.

[47] K.Y. Dai, G.R. Liu, X. Han, Y. Li, Inelastic analysis of 2D solids using a weak-form RPIM based on deformation theory, Comput. Methods Appl. Mech. Engrg. 195 (2006) 4179–4193.

[48] R.L. Hardy, Theory and applications of the multiquadrics – biharmonic method (20 years of discovery 1968–1988), Comput. Math. Appl. 19 (1990) 127–161.

[49] M.A. Golberg, C.S. Chen, H. Bowman, Some recent results and proposals for the use of radial basis functions in the BEM, Engrg. Anal. Boundary Elements 23 (1999) 285–296.

[50] G.R. Liu, Y.T. Gu, K.Y. Dai, Assessment and applications of interpolation methods for computational mechanics, Int. J. Numer. Methods Engrg. 59 (2004) 1373–1379.

[51] S. Timoshenko, J.N. Goodier, Theory of Elasticity, third ed., McGraw Hill, 1970.

[52] B.M. Irons, A. Razzaque, Experience with the patch test for convergence of nite elements, in: A.K. Aziz (Ed.), The Mathematical Foundations of the Finite Element Method with Applications to Partial Differential Equations, Academic Press, New York, 1972.